I. Systems Analysis Research

SYSTEMS DIVISION

A. A Solar Electric Propulsion Spacecraft Asteroid Probe, *C. G. Sauer*

1. Introduction

In the past several years a number of studies have been made in determining the applicability of solar-electric-propulsion (SEP) spacecraft to the unmanned scientific investigation of the solar system.

This article presents several trajectory and spacecraft parameters f .. a solar-electric-propulsion spacecraft that could be used as a deep-space asteroid probe. The purposes of this mission would be to make: (1) an engineering test flight of a spacecraft using electric-propulsion thrustors and lightweight rollout solar panels as a power source, and (2) a scientific investigation of the region of the solar system encompassing 2 to 3 AU, including the asteroid belt. A minimum thrustor operating time of 400 days at an initial power level of approximately 4.6 kW at 1 AU is desired.

2. Spacecraft Description

The launch vehicle proposed for this mission is an *Atlas SLV3C/Centaur* with an injected weight capability at escape of 2500 lb. The SEP spacecraft would have a mass of 750 lb, not including the solar panels, thrustors, and power-conditioning subsystems. The "installed" power capability of the solar panels proposed for this spacecraft is 6 kW at 1 AU; however, an assumed 18% degradation due to solar flares and environmental uncertainties results in a net power capability of 4.92 kW. Of this amount, 320 W is reserved for spacecraft auxilliary purposes, leaving a net thrustor input power at 1 AU of 4.6 kW. In the data to be presented, a total spacecraft mass of 480 kg was used, not including the low-thrust propellant mass.

The mission profile consists of a spacecraft injection at a *vis viva* energy of C_3 equal to 10 to 16 km^2/s^2. The spacecraft is injected so that the hyperbolic velocity is aligned in the direction of the motion of the earth and in the ecliptic plane. Shortly after injection, the spacecraft would be aligned so that the SEP engines will be thrusting in a direction normal to the sun line and in the ecliptic plane. Since a specific target has not been identified, the selection of a launch date at this time is somewhat arbitrary; consequently, the trajectories shown in this analysis were initiated with an initial heliocentric longitude of zero corresponding to a launch date late in September.

The required propellant mass, exclusive of residuals, is shown in Fig. 1 as a function of departure C_3 for propulsion times of 400, 500, and 600 days. Since the propellant mass flow rate is directly proportional to thrustor input power, the mass flow rate will decrease with increasing probe distance from the sun because of the drop in power

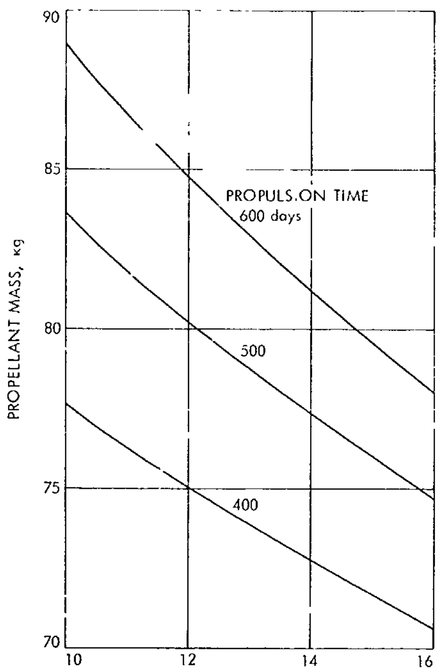

Fig. 1. SEP spacecraft asteroid probe, propellant mass versus C_3

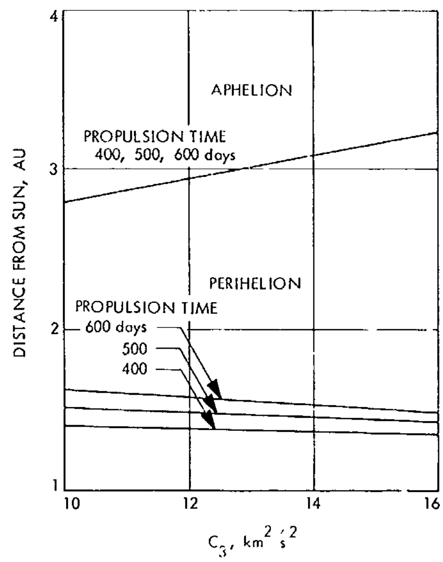

Fig. 2. SEP spacecraft asteroid probe, aphelion and perihelion distance versus C_3

from the solar panels. The additional propellant required for thrusting an additional 100 to 200 days is relatively small, since the available power to the thrustors and also the propellant flow rate has dropped to about one sixth of the initial value after 400 to 500 days. An additional 100 days of propulsion requires, at most, 5 kg additional propellant (Fig. 1).

3. Trajectory Characteristics

The aphelion and perihelion of the heliocentric trajectory after thrust cutoff is shown in Fig. 2 as a function of departure C_3. The effect of increasing the propulsion time does not materially affect the aphelion distance since thrust cutoff occurs near this point, and additional thrusting has the effect of raising the perihelion but does not affect the aphelion distance. The aphelion distance does increase with increasing C_3, however, and an aphelion range of 2¾ to 3¼ AU can be covered with a departure C_3 in the range of 10 to 16 km^2/s^2. The perihelion distance decreases slightly with increasing C_3 and increases with an increase in propulsion time.

The path of the spacecraft in the ecliptic plane is shown in Figs. 3 and 4 for a propulsion time of 400 days and for departure *vis viva* energies of 10 and 16 km^2/s^2. Figure 3 shows the path of the vehicle for a departure C_3 of 10 km^2/s^2. The probe spends 250 days to 950 days beyond 2 AU with aphelion occurring at 600 days. In Fig. 4 the path of the spacecraft for a departure C_3 of 16 km^2/s^2 remains beyond 2 AU for 210 days to 1110 days or for a total of 900 days as compared with the 700 days for the trajectory shown in Fig. 3.

The power available to the thrustors is shown in Fig. 5 as a function of time along the trajectory. Because of thrustor design considerations, it would seem inadvisable to operate the low-thrust engines at a power level less than around ½ kW. For a trajectory with a departure C_3 of 16 km^2/s^2 this point occurs at about 400 days, and in order to provide additional operating time, the motors could be restarted at about 900 days. The second trajectory, corresponding to a C_3 of 10 km^2/s^2, has a minimum power of ½ kW at aphelion.

4. Communication Parameters

Figure 6 presents the communication distance as a function of time for the same trajectories used previously. A communication distance of 530 to 560 million km is required to observe the thrust cutoff point at 400 days. Delaying thrust cutoff until 600 days will reduce the communication distance by about a factor of 2. An interesting feature of the trajectory shown in Fig. 3 for a C_3 of 10 km^2/s^2 is that it is close to being synchronous with the period of the earth—quite close to 3 yr. Opposition with the earth occurs close to aphelion and perihelion of the spacecraft trajectory.

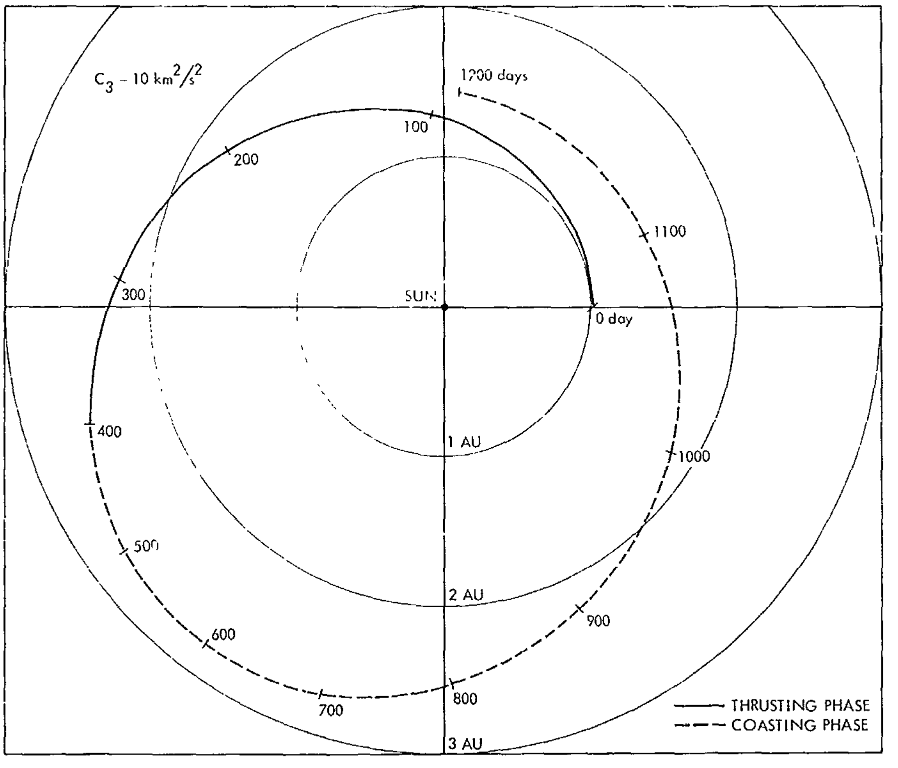

Fig. 3. SEP spacecraft asteroid probe, $C_3 = 10\ km^2/s^2$

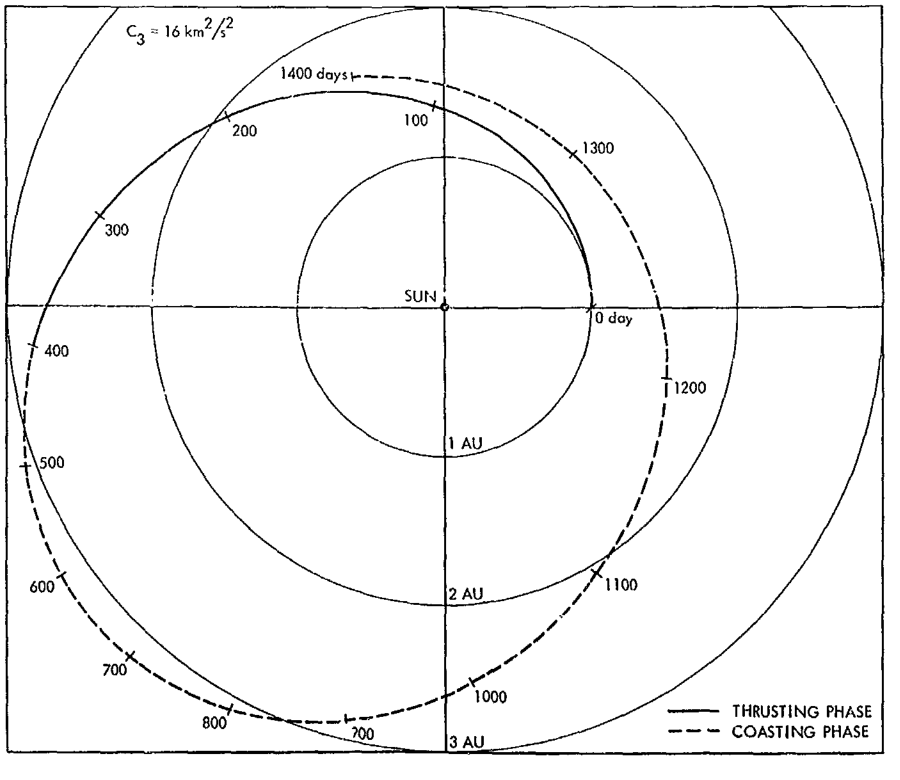

Fig. 4. SEP spacecraft asteroid probe, $C_3 = 16\ km^2/s^2$

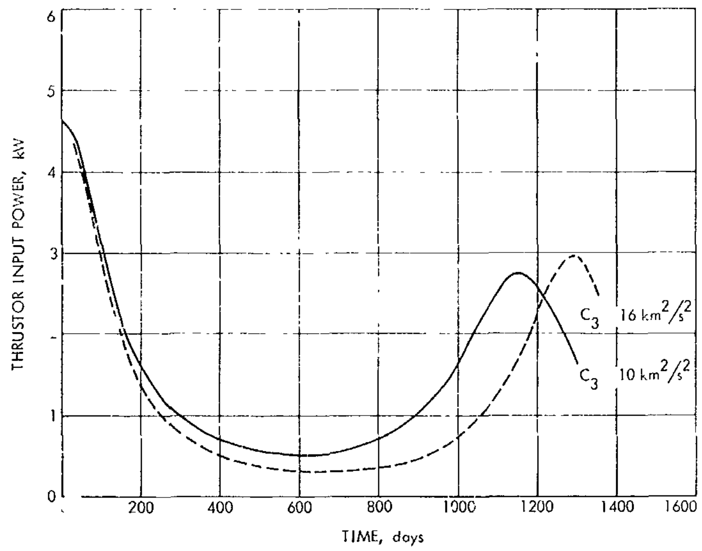

Fig. 5. SEP spacecraft asteroid probe thrustor input power

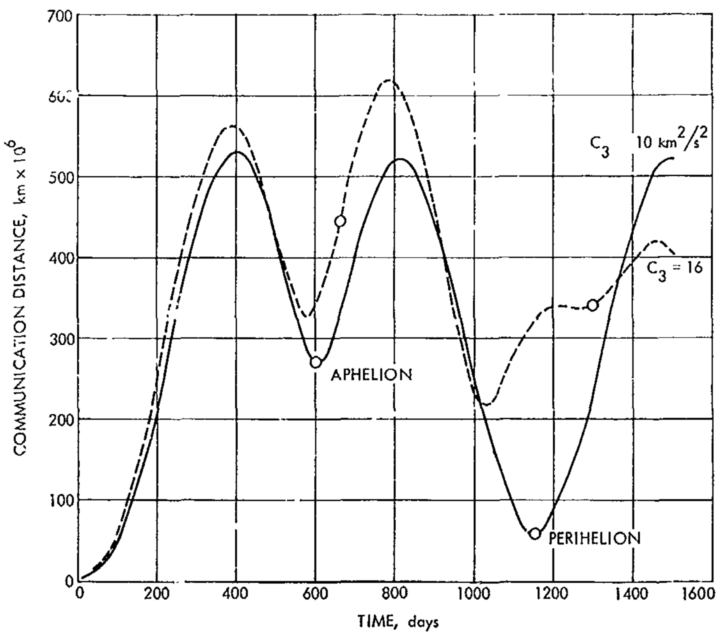

Fig. 6. SEP spacecraft asteroid probe communication distance versus time

The antenna direction, given by the earth-probe-sun angle, is shown in Fig. 7 as a function of time. Excluding the initial 60 to 70 days, a maximum antenna direction from the sun line of not more than 35 deg is required for the duration of the mission. Initially this angle is around 90 deg as the probe recedes from the earth in the direction of the motion of the earth. At the point where the earth-probe-sun angle has decreased to 35 deg, the communication distance is around 15 million km.

B. Progress Toward a Numerically Integrated Lunar Ephemeris, *D. B. Holdridge and J. D. Mulholland*

For the past year it has been evident that the high accuracy required of the lunar ephemeris, if it is to achieve maximum utility in the analysis of spacecraft data, can be obtained at the present time only by numerical integration of the equations of motion (Ref. 1). The imple-

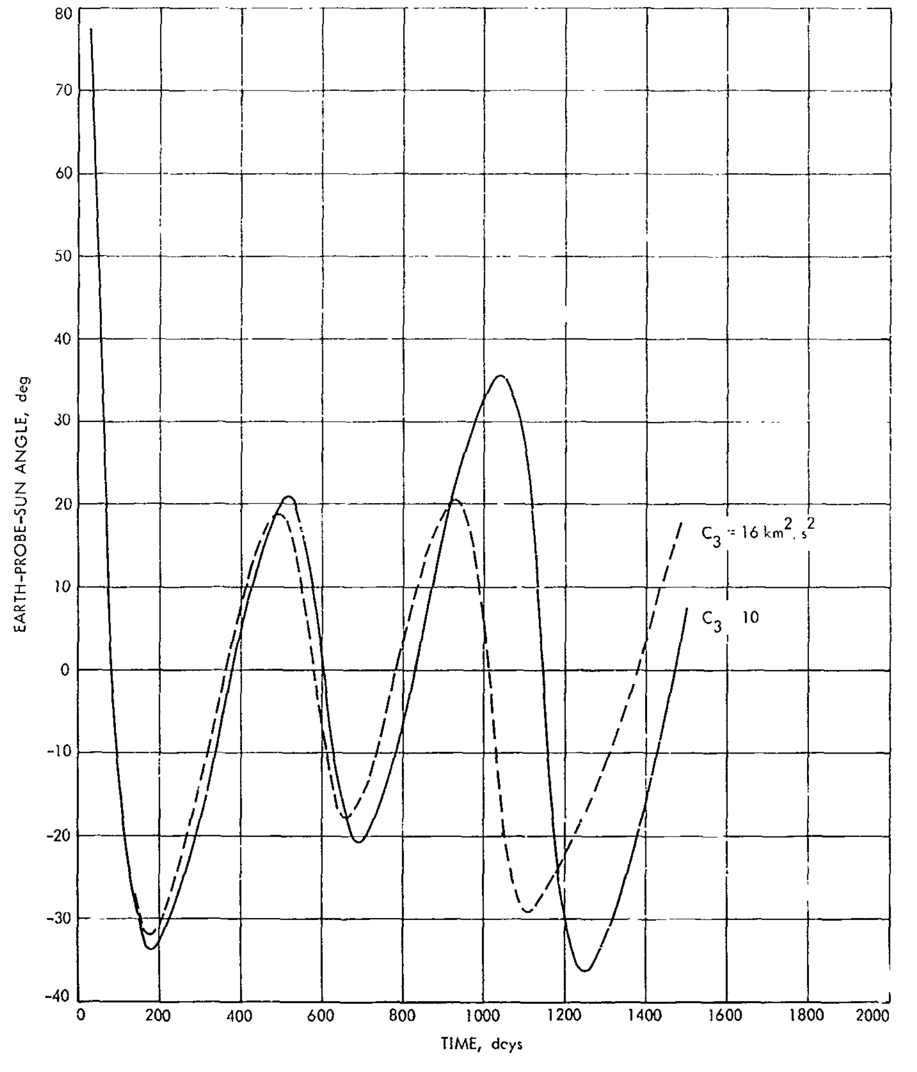

Fig. 7. SEP spacecraft asteroid probe earth–probe–sun angle

mentation of such an ephemeris has been pursued in two conceptually distinct, but complementary, phases.

1. Numerical Fit to Theory

The work that was reported in Ref. 1 and in SPS 37-49, Vol. III, pp. 13–15, consisted of a single-body integration of the lunar orbit over a 2-yr interval, differentially corrected to fit the theory-based ephemeris designated LE 4 (Ref. 2) by means of a modified version of the planetary orbit determination program (PLOD; Ref. 3). After it was established that serious defects existed in the theoretical ephemeris, an effort was mounted for the extension of this work to a meaningful time span. To properly treat the long-term characteristics of the motion, the nodal period (18.6 yr) may be regarded as a practical minimum interval over which to extend the differential correction procedure. The interval actually adopted was from JED 243 3280.5 to 244 0800.5, slightly more than 20 yr, beginning at the epoch of the JPL ephemeris tape system.

There are several arguments in favor of producing acceptable fits to the theoretical ephemeris as a prior step to dealing with the observations. The most cogent one in the early stages of the work was the ease and rapidity with which the PLOD program could be modified to perform this task. At present, it is far more important that this process can be regarded as a controlled experiment that will permit the development of techniques for solving the real problems of fitting the lunar motion without introducing the uncertainties and biases that always accompany observational data. Despite its flaws, the Lunar Theory does conform rather well to the real motion of the moon, particularly in those features that are a hindrance to the production of an accurate ephemeris by numerical integration. These features primarily affect two aspects: (1) the differential correction and, (2) the modeling of effects that arise from other than point-mass gravitational considerations.

The moon is a highly perturbed object, and the standard differential correction procedures used in PLOD, as in other planetary ephemeris development programs, are based on formulas that assume Keplerian motion. This is acceptable in the planetary case, because the planets are remarkably well behaved. In the attempts to extend the correction span beyond 2 yr, the suspicion was amply confirmed that the unperturbed partial derivatives are not adequate in the lunar case. Successive corrections for a series of 5-yr integrations failed to converge to a final set of initial conditions.

The possible ways in which one could produce perturbed partial derivatives were discussed in an earlier article (SPS 37-51, Vol. III, pp. 13–15), and a detailed discussion was given of the implementation of one of the alternatives, that of analytic series expressions. Subsequent to the writing of that article, discussions[1] revealed that the expressions for $a\partial\hat{s}/\partial a$ referred only to the scale factor effect and did not include the dynamical effect (Ref. 4, p. 235) involving the angular motion. It would become necessary to introduce this effect into the computation of $[\partial\kappa_0/\partial\kappa_1]$, and much of the estimated saving in computer running time would have disappeared, in addition to the programming effort that this approach would have entailed. As a consequence, the relatively simple method of finite difference quotients was eventually used for the partial derivative computations.

The availability of reasonably accurate partial derivatives resolved the differential correction problem, and within a relatively short time a converged series of integrated fits over the 20-yr span was obtained, the source theory being LE 6 (Ref. 5). Although the correction series did converge to a final solution, the residuals of that solution were not really satisfactory, and the reason for this situation is believed to lie in the modeling problem.

The major flaw in using a theory as the comparison base for a numerical integration is the possibility that empirical adjustments to the theory may destroy the faithfulness with which it reflects the nominal model on which it was constructed. In the case of the Lunar Theory and our integrations, the tides, the figure of the moon, and perhaps some yet unknown cause have led to such adjustments. In each case, analysis of the observational data showed one or more of the orbital parameters to be inadequately represented by the theory, and in each case the theoretical expressions were replaced by the observational values. The numerical integrations are based on gravitational models not greatly different from that on which the theory is founded, so one would not expect these empirical aspects of the theory to be properly modeled in the integration. It is necessary either to learn how to model them or how to handle such empirical fixes in conjunction with a numerical integration.

Such a component in the lunar motion is attributed to the frictional losses in the tidal deformations of earth. These losses reduce the rotational angular momentum of earth, with subsequent gain in the orbital angular momentum of moon. This gain is reflected in a secular increase in the mean distance and decrease in the sidereal mean motion. This is represented as a secular acceleration of the mean longitude

$$\Delta L = -11''\!.22\, T^2$$

where T is measured in Julian centuries. There is less than complete agreement on the detailed mechanism of this angular momentum transfer, but it is widely assumed (e.g., Ref. 6) that it involves the gravitational couple generated by the tidal bulge. Whatever the mechanism, it is not modeled in the differential equations of motion, and a means must be found of treating the real phenomenon.

Both the perigee and the node have motions that arise from unmodeled causes. The current ephemeris programs treat the moon as a point of mass, whereas the Brown theory embodies a triaxial moon not greatly different from the one currently recommended. The solar system data-processing system is to be modified to include this feature, but in the interim, it is necessary to find an empirical way of treating the motions. Such an empirical treatment is necessary from another aspect, too. Eckert (Ref. 7) has shown that the present observational values of $d\tilde{\omega}/dT$ and $d\Omega/dT$ cannot be satisfied with the present model without assuming an unbelievable lunar density distribution. That is, the perigee and node have motions that *cannot* be modeled in the light of present knowledge. These last two effects combined amount to

$$\Delta\tilde{\omega} = -3''\!.1\, T, \qquad \Delta\Omega = -27''\!.9\, T$$

[1]With T. C. Van Flandern, U.S. Naval Observatory, who developed the analytic partial derivatives.

There seems to be no simple resolution of this within the structure of PLOD.

As a means of discovering if these various effects are the cause of the remaining large-scale residuals in the PLOD integrations of the lunar motion, a theoretical ephemeris (LE 12) has been constructed by removing the gravitationally unmodeled effects from LE 6. Numerical integrations fit to this ephemeris are now under way.

2. Use of Lunar Observations

In the long run the fitting of theories must be abandoned, and one must return to the source of all empirical knowledge—the observations. The modifications necessary to convert the solar system data-processing system (SPS 37-51, Vol. III, pp. 4-1?) to lunar application are now being programmed. Many gains are expected from this. The figure of the moon can be modeled; perhaps the tidal effect can be modeled. It may even be that the unexplained defect of the theory noted above is not due to the figure of the moon at all, but to the currently accepted observational values. A recent analysis of the occultation observations[2] seems to suggest that this is a possibility. If so, this discrepancy should disappear with the use of observational data.

---

[2]Martin, C. F., "ET-UT Time Corrections for the Period 1627–1860," in *Observation, Analysis and Space Research Applications of the Lunar Motion*. Edited by J. D. Mulholland (in preparation).

References

1. Mulholland, J. D., and Devine, C. J., "Gravitational Inconsistency in the Lunar Theory: Numerical Determination," *Science*, Vol. 160, pp. 874–875, May 24, 1968.

2. Mulholland, J. D., and Block, N., *JPL Lunar Ephemeris Number 4* Technical Memorandum 33-346. Jet Propulsion Laboratory, Pasadena, Calif., August 1, 1967.

3. Devine, C. J., *PLOD II: Planetary Orbit Determination Program for the IBM 7094 Computer* Technical Memorandum 33-188. Jet Propulsion Laboratory, Pasadena, Calif., April 15, 1965.

4. Brouwer, D., and Clemence, G. M., *Methods of Celestial Mechanics*. Academic Press, New York, 1961.

5. Mulholland, J. D., *JPL Lunar Ephemeris Number 6* Technical Memorandum 33-408. Jet Propulsion Laboratory, Pasadena, Calif., October 15, 1968.

6. Gerstenkorn, H., "The Model of the So-Called 'Weak' Tidal Friction and the Limits of Its Applicability" in *Mantles of the Earth and Terrestrial Planets*. Edited by S. K. corn. Interscience Publishers, Inc., London, 1967.

7. Eckert, W. J., "On the Motions of Perigee and Node and the Distribution of Mass in the Moon," *Astron. J.*, Vol. 70, pp. 787–792, 1965.

C. Effect of Precession and Nutation Errors on Radar Observations, *J. H. Lieske*

The partial derivatives relating errors in the constant of general precession in longitude and the constant of nutation to changes in range and range rate are developed in this article. It will be shown that an error on the order of 1 arc sec/century in the general precession in longitude will introduce drifts on the order of 30 m/century in range and 2 mm/s/century in range rate. The effect probably will be absorbed by station longitude and would amount to a drift on the order of 1/3 m/yr. Errors in the constant of nutation, on the other hand, introduce effects on the order of 600 mm and 0.04 mm/s on the range and range rate, respectively, for an error in the coefficient of nutation of 0.01 arc sec. The partial derivatives will be developed in an equatorial 1950.0 frame, and simplified expressions adequate for most purposes will be given.

In the present investigation it is assumed that the vector $\boldsymbol{\rho}$ from the observer to the object being tracked is given by the expression

$$\boldsymbol{\rho} = \mathbf{r} - \mathbf{R}_e - \mathbf{A}_P^T \mathbf{A}_N^T \mathbf{R}_S \tag{1}$$

where $\mathbf{r}$ and $\mathbf{R}_e$ are the heliocentric vectors to the object and to the center of the earth referred to the equator and equinox of 1950.0, respectively, and $\mathbf{A}_P^T \mathbf{A}_N^T \mathbf{R}_S$ is the vector from the geocenter to the observer in a 1950.0 frame. The transpose of a matrix $\mathbf{A}$ is denoted by $\mathbf{A}^T$. The precession matrix $\mathbf{A}_P$ and nutation matrix $\mathbf{A}_N$ are given by the usual expressions (Ref. 1)

$$\mathbf{A}_P = \begin{bmatrix} \cos\zeta_0\cos\theta\cos z - \sin\zeta_0\sin z & -\sin\zeta_0\cos\theta\cos z - \cos\zeta_0\sin z & -\sin\theta\cos z \\ \cos\zeta_0\cos\theta\sin z + \sin\zeta_0\cos z & -\sin\zeta_0\cos\theta\sin z + \cos\zeta_0\cos z & -\sin\theta\sin z \\ \cos\zeta_0\sin\theta & -\sin\zeta_0\sin\theta & \cos\theta \end{bmatrix} \tag{2}$$

$$
\mathbf{A}_N = \begin{bmatrix} \cos\Delta\psi & -\cos\bar{\epsilon}\sin\Delta\psi & -\sin\Delta\psi\sin\bar{\epsilon} \\ \sin\Delta\psi\cos\epsilon & \cos\Delta\psi\cos\bar{\epsilon}\cos\epsilon + \sin\bar{\epsilon}\sin\epsilon & \cos\Delta\psi\sin\bar{\epsilon}\cos\epsilon - \cos\bar{\epsilon}\sin\epsilon \\ \sin\Delta\psi\sin\epsilon & \cos\Delta\psi\cos\bar{\epsilon}\sin\epsilon - \sin\bar{\epsilon}\cos\epsilon & \cos\Delta\psi\sin\bar{\epsilon}\sin\epsilon + \cos\bar{\epsilon}\cos\epsilon \end{bmatrix} \tag{3}
$$

where ζ_0, z, and θ are the precession parameters employed in reducing positions referred to the mean equator and equinox of 1950.0 to the mean equator and equinox of date, where $\Delta\psi$ is the nutation in longitude, and ϵ and $\bar{\epsilon}$ refer to the true and mean obliquity of the ecliptic of date, respectively. The geocentric position of the observer referred to the true equator and equinox of date is assumed to be in the form

$$
\mathbf{R}_S = \begin{bmatrix} \cos\theta_G & -\sin\theta_G & 0 \\ \sin\theta_G & \cos\theta_G & 0 \\ 0 & 0 & 1 \end{bmatrix} \mathbf{S} \tag{4}
$$

where θ_G is the true Greenwich sidereal time, and

$$
\mathbf{S} = \begin{bmatrix} R_0 \cos\phi' \cos\lambda_E \\ R_0 \cos\phi' \sin\lambda_E \\ R_0 \sin\phi' \end{bmatrix} \tag{5}
$$

with R_0 representing the geocentric distance of the observer; ϕ', his geocentric latitude, and λ_E, the observer's longitude measured east from Greenwich.

An important and useful property of these orthogonal rotation matrices is that if $\mathbf{A}$ is a rotation matrix, or the matrix product of several orthogonal matrices, and if q is a parameter upon which one or several of the matrices depend, then the matrix

$$
\mathbf{C} = \frac{\partial \mathbf{A}^T}{\partial q}\mathbf{A}
$$

is skew-symmetric, or the sum of several skew-symmetric matrices, and hence the quadratic form

$$
B = \mathbf{x}^T \mathbf{C} \mathbf{x} \tag{6}
$$

is zero for any vector $\mathbf{x}$. This property is useful in obtaining the partial derivative of the scalar slant range $\partial\rho/\partial q$ from the vectors $\boldsymbol{\rho}$ and $\partial\boldsymbol{\rho}/\partial q$. As an example, consider the contribution of $\partial\boldsymbol{\rho}/\partial q$ to the desired quantity $\partial\rho/\partial q$.

If $\mathbf{A}_N$ and $\mathbf{A}_P$ depend upon the parameter q, then

$$
\frac{\partial\boldsymbol{\rho}}{\partial q} = -\left(\frac{\partial \mathbf{A}_P^T}{\partial q}\mathbf{A}_N^T + \mathbf{A}_P^T \frac{\partial \mathbf{A}_N^T}{\partial q}\right)\mathbf{R}_S
$$

$$
\begin{aligned}
\rho\frac{\partial \rho}{\partial q} &= (\mathbf{r} - \mathbf{R}_e - \mathbf{A}_P^T\mathbf{A}_N^T\mathbf{R}_S)^T \\
&\quad \times\left(-\frac{\partial \mathbf{A}_P^T}{\partial q}\mathbf{A}_N^T - \mathbf{A}_P^T\frac{\partial \mathbf{A}_N^T}{\partial q}\right)\mathbf{R}_S \\
&= -(\mathbf{r} - \mathbf{R}_e)^T\left(\frac{\partial \mathbf{A}_P^T}{\partial q}\mathbf{A}_N^T + \mathbf{A}_P^T\frac{\partial \mathbf{A}_N^T}{\partial q}\right)\mathbf{R}_S \\
&\quad + \mathbf{R}_S^T\mathbf{A}_N\mathbf{A}_P\frac{\partial \mathbf{A}_P^T}{\partial q}\mathbf{A}_N^T\mathbf{R}_S + \mathbf{R}_S^T\mathbf{A}_N\frac{\partial \mathbf{A}_N^T}{\partial q}\mathbf{R}_S .
\end{aligned}
$$

The skew-symmetric property may be used to show that the last two terms in the above equation are zero because

$$
\mathbf{A}_P\frac{\partial \mathbf{A}_P^T}{\partial q}
$$

is skew-symmetric, as is

$$
\mathbf{A}_N\left(\mathbf{A}_P\frac{\partial \mathbf{A}_P^T}{\partial q}\right)\mathbf{A}_N^T
$$

Hence, the quadratic form

$$
\mathbf{R}_S^T\left(\mathbf{A}_N\mathbf{A}_P\frac{\partial \mathbf{A}_P^T}{\partial q}\mathbf{A}_N^T\right)\mathbf{R}_S
$$

is zero. The same comments apply for

$$
\mathbf{R}_S^T\mathbf{A}_N\frac{\partial \mathbf{A}_N^T}{\partial q}\mathbf{R}_S
$$

Since there are several forms one may wish to employ for the computed range or doppler, the skew-symmetric property will be extremely useful in computing the various forms. In the remainder of this paper only the vector partial derivatives $\partial\boldsymbol{\rho}/\partial q$ and $\partial\dot{\boldsymbol{\rho}}/\partial q$ will be computed, so that a person may combine them in whatever type of range or doppler equation he desires.

It is clear that the heliocentric positions $\mathbf{r}$ of the planet and $\mathbf{R}_e$ of the earth referred to the 1950.0 equator and equinox will not depend upon the values of precession and nutation (although their estimated values certainly are affected to some extent). We thus need only be concerned with the effect of precession and nutation on $\mathbf{A}_P$, $\mathbf{A}_N$ and $\mathbf{R}_S$ of the observer. The observer's geocentric position $\mathbf{R}_S$ is affected by precession and nutation only through the sidereal time, as indicated by Eq. (4). The true Greenwich sidereal time θ_G is of the form

$$\theta_G = \bar{\theta}_G + \Delta\psi \cos \epsilon + \delta \tag{7}$$

where $\bar{\theta}_G$ is the mean Greenwich sidereal time and δ includes the effects of polar motion, annual periodic variations, etc. While it is true that the origin of the definition of mean Greenwich sidereal time $\bar{\theta}_G$ involved introducing a specific value of the general precession in right ascension, the expression for $\bar{\theta}_G$ is now to be taken *as a definition* of the universal time; hence $\bar{\theta}_G$ will not be affected by any error in precession, since it is *defined* as the Greenwich hour angle of the mean equinox of date. We then see that the true sidereal time is affected by nutation but not precession.

The partial derivatives of ζ_0, z, and θ appearing in Eq. (2) with respect to the general precession in longitude p are taken from Lieske (Ref. 2):

$$\left.\begin{aligned} \frac{\partial \zeta_0}{\partial p} &= \frac{\partial z}{\partial p} = 0.45891T = \frac{T}{2}\cos\epsilon_0 \\ \frac{\partial \theta}{\partial p} &= 0.39780T = T \sin\epsilon_0 \end{aligned}\right\} \tag{8}$$

where T is measured in tropical centuries from 1950.0, and ϵ_0 is the mean obliquity of the ecliptic at 1950.0. The nutation in obliquity is assumed to be of the form

$$\Delta\epsilon = \epsilon - \bar{\epsilon} = N \cos \Omega_☾ \tag{9}$$

while the nutation in longitude is taken as

$$\Delta\psi = -\gamma N \sin \Omega_☾ \tag{10}$$

where $N = 9\rlap{.}''210$, $\gamma = 1.8712$ (so that $-\gamma N = -17\rlap{.}''234$) and where $\Omega_☾$ is the node of the orbit of the moon on the mean ecliptic of date.

The partial derivatives required for general precession in longitude are

$$\frac{\partial \boldsymbol{\rho}}{\partial p} = -\frac{\partial \mathbf{A}_P^T}{\partial p}\mathbf{A}_N^T \mathbf{R}_S \tag{11}$$

$$\frac{\partial \dot{\boldsymbol{\rho}}}{\partial p} = -\frac{\partial \mathbf{A}_P^T}{\partial p}\mathbf{A}_N^T \dot{\mathbf{R}}_S - \left(\frac{\partial \dot{\mathbf{A}}^T}{\partial p}\mathbf{A}_N^T + \frac{\partial \mathbf{A}_P^T}{\partial p}\dot{\mathbf{A}}_N^T\right)\mathbf{R}_S \tag{12}$$

while those for nutation are

$$\frac{\partial \boldsymbol{\rho}}{\partial N} = -\mathbf{A}_P^T \frac{\partial \mathbf{A}_N^T}{\partial N}\mathbf{R}_S - \mathbf{A}_P^T\mathbf{A}_N^T\frac{\partial \mathbf{R}_S}{\partial N} \tag{13}$$

$$\begin{aligned} \frac{\partial \dot{\boldsymbol{\rho}}}{\partial N} = &- \mathbf{A}_P^T \frac{\partial \mathbf{A}_N^T}{\partial N}\dot{\mathbf{R}}_S - \mathbf{A}_P^T\mathbf{A}_N^T\frac{\partial \dot{\mathbf{R}}_S}{\partial N} \\ &- \left(\dot{\mathbf{A}}_P^T \frac{\partial \mathbf{A}_N^T}{\partial N} + \mathbf{A}_P^T \frac{\partial \dot{\mathbf{A}}^T}{\partial N}\right)\mathbf{R}_S \\ &- \left(\dot{\mathbf{A}}_P^T\mathbf{A}_N^T + \mathbf{A}_P^T\dot{\mathbf{A}}_N^T\right)\frac{\partial \mathbf{R}_S}{\partial N} \end{aligned} \tag{14}$$

The matrices $\mathbf{A}_P$, $\mathbf{A}_N$, and $\mathbf{R}_S$ are already defined in Eqs. (2), (3), (4) and (5), and their partial derivatives may be readily computed. Simplified forms, adequate for most purposes, will be given later. The complete forms will be given in order that one may employ the more exact relations if he so desires.

The matrix $\partial \mathbf{A}_P/\partial p$ is determined from

$$\frac{\partial \mathbf{A}_P}{\partial p} = \frac{\partial \mathbf{A}_P}{\partial \zeta_0}\frac{\partial \zeta_0}{\partial p} + \frac{\partial \mathbf{A}_P}{\partial z}\frac{\partial z}{\partial p} + \frac{\partial \mathbf{A}_P}{\partial \theta}\frac{\partial \theta}{\partial p} \tag{15}$$

where

$$\frac{\partial \zeta_0}{\partial p}, \frac{\partial z}{\partial p}, \frac{\partial \theta}{\partial p}$$

are given by Eq. (8).

The partial derivative of the nutation matrix $\mathbf{A}_N$ with respect to the constant of nutation N is given by

$$\frac{\partial \mathbf{A}_N}{\partial N} = -\gamma \sin \Omega_☾ \frac{\partial \mathbf{A}_N}{\partial (\Delta\psi)} + \cos \Omega_☾ \frac{\partial \mathbf{A}_N}{\partial \epsilon} \tag{16}$$

where $\gamma = 1.8712$.

Before computing the partial derivatives of ρ and $\dot{\rho}$ with respect to p and N we still need $\partial \mathbf{R}_S/\partial N$. The required relation is found by combining Eqs. (4), (7), and (10). The result is

$$\frac{\partial \mathbf{R}_S}{\partial N} = -\gamma \sin \Omega_{\mathbb{C}} \cos \epsilon \frac{\partial \mathbf{R}_S}{\partial \theta_G} \qquad (17)$$

From Eqs. (11) to (14) combined with Eqs. (8) and (15) to (17) one can then obtain $\partial \rho/\partial p$, $\partial \dot{\rho}/\partial p$, $\partial \rho/\partial N$, and $\partial \dot{\rho}/\partial N$. However, an examination of the maximum effect of each of the terms in Eqs. (11) through (14) upon ρ and $\dot{\rho}$ shows that several of the matrices may be neglected, and others may be simplified. In estimating the effects of the terms upon $\Delta\rho$ and $\Delta\dot{\rho}$, it is assumed that the error in general precession in longitude is approximately 1 arc sec per century (Refs. 3, 4) while that in the nutation coefficient is 0.01 arc sec (Ref. 5).

The effects of $\Delta p = 1$ arc sec per century on ρ and $\dot{\rho}$ are approximately:

For $\Delta\rho$

$$\frac{\partial \mathbf{A}_P^T}{\partial p} \mathbf{A}_N^T \mathbf{R}_S \Delta p \sim 30 \text{ m/century}$$

and for $\Delta\dot{\rho}$

$$\frac{\partial \mathbf{A}_P^T}{\partial p} \mathbf{A}_N^T \dot{\mathbf{R}}_S \Delta p \sim 2 \text{ mm/s/century}$$

$$\frac{\partial \dot{\mathbf{A}}^T}{\partial p} \mathbf{A}_N^T \mathbf{R}_S \Delta p \sim 5 \times 10^{-7} \text{ mm/s/century}$$

$$\frac{\partial \mathbf{A}_P^T}{\partial p} \dot{\mathbf{A}}_N^T \mathbf{R}_S \Delta p \sim 1 \times 10^{-7} \text{ mm/s/century}$$

while the effects of $\Delta N = 0''.01$ upon ρ and $\dot{\rho}$ are approximately:

For $\Delta\rho$

$$\mathbf{A}_P^T \frac{\partial \mathbf{A}_N^T}{\partial N} \mathbf{R}_S \Delta N \sim 600 \text{ mm}$$

$$\mathbf{A}_P^T \mathbf{A}_N^T \frac{\partial \mathbf{R}_S}{\partial N} \Delta N \sim 600 \text{ mm}$$

and for $\Delta\dot{\rho}$

$$\mathbf{A}_P^T \frac{\partial \mathbf{A}_N^T}{\partial N} \dot{\mathbf{R}}_S \Delta N \sim 4 \times 10^{-2} \text{ mm/s}$$

$$\mathbf{A}_P^T \mathbf{A}_N^T \frac{\partial \dot{\mathbf{R}}_S}{\partial N} \Delta N \sim 4 \times 10^{-2} \text{ mm/s}$$

$$\dot{\mathbf{A}}_P^T \frac{\partial \mathbf{A}_N^T}{\partial N} \mathbf{R}_S \Delta N \sim 5 \times 10^{-9} \text{ mm/s}$$

$$\mathbf{A}_P^T \frac{\partial \dot{\mathbf{A}}_N^T}{\partial N} \mathbf{R}_S \Delta N \sim 1 \times 10^{-9} \text{ mm/s}$$

$$\dot{\mathbf{A}}_P^T \mathbf{A}_N^T \frac{\partial \mathbf{R}_S}{\partial N} \Delta N \sim 5 \times 10^{-9} \text{ mm/s}$$

$$\mathbf{A}_P^T \dot{\mathbf{A}}_N^T \frac{\partial \mathbf{R}_S}{\partial N} \Delta N \sim 1 \times 10^{-9} \text{ mm/s}$$

In light of the preceding estimates, we may neglect the terms in parentheses in Eqs. (11) through (14) and may use only the largest terms in the remaining matrices. With these simplifications the partial derivatives for precession reduce to

$$\left.\begin{aligned} \frac{\partial \rho}{\partial p} &= \mathbf{C}_P \mathbf{R}_S \\ \frac{\partial \dot{\rho}}{\partial p} &= \mathbf{C}_P \dot{\mathbf{R}}_S \end{aligned}\right\} \qquad (18)$$

where

$$\mathbf{C}_P = \begin{bmatrix} 0 & -T\cos\epsilon_0 & -T\sin\epsilon_0 \\ T\cos\epsilon_0 & 0 & 0 \\ T\sin\epsilon_0 & 0 & 0 \end{bmatrix}$$

and where T is the time in centuries from 1950.0, and ϵ_0 is the obliquity of the ecliptic at 1950.0.

The simplified expressions for the partial derivatives with respect to the constant of nutation are

$$\frac{\partial \rho}{\partial N} = \mathbf{C}_N \mathbf{S}$$

$$\frac{\partial \dot{\rho}}{\partial N} = \dot{\theta}_G \frac{\partial \mathbf{C}_N}{\partial \theta_G} \mathbf{S} \qquad (19)$$

where

$$
\mathbf{C}_N = \begin{bmatrix} 0 & 0 & \gamma \sin \epsilon \sin \Omega_{☾} \\ 0 & 0 & -\cos \Omega_{☾} \\ -\gamma \sin \epsilon \sin \Omega_{☾} \cos \theta_G + \sin \theta_G \cos \Omega_{☾} & \gamma \sin \epsilon \sin \Omega_{☾} \sin \theta_G + \cos \theta_G \cos \Omega_{☾} & 0 \end{bmatrix}
$$

and where $\dot{\theta}_G$ may be taken as 2π rad/86,400 s with sufficient accuracy.

For most applications, Eqs. (18) and (19) will be adequate for representation of the effects of errors in precession and nutation upon $\boldsymbol{\rho}$ and $\dot{\boldsymbol{\rho}}$. If higher precision is desired, one may use the actual matrices such as $\partial \mathbf{A}_N / \partial p$ and $\partial \mathbf{A}_N / \partial N$.

With the above approximations, it is seen that the expression for $\partial \rho / \partial p$ is of the form

$$
\rho \frac{\partial \rho}{\partial p} = \boldsymbol{\rho}^T \begin{bmatrix} 0 & -T \cos \epsilon_0 & -T \sin \epsilon_0 \\ T \cos \epsilon_0 & 0 & 0 \\ T \sin \epsilon_0 & 0 & 0 \end{bmatrix} \mathbf{R}_S \tag{20}
$$

while the partial derivative of the slant range with respect to the observer's longitude is of the form

$$
\rho \frac{\partial \rho}{\partial \lambda_E} = \boldsymbol{\rho}^T \begin{bmatrix} 0 & +1 & 0 \\ -1 & 0 & 0 \\ 0 & 0 & 0 \end{bmatrix} \mathbf{R}_S \tag{21}
$$

and the partial derivative with respect to the observer's latitude is of the form

$$
\rho \frac{\partial \rho}{\partial \phi'} = \boldsymbol{\rho}^T \begin{bmatrix} 0 & 0 & \cos (\theta_G + \lambda_E) \\ 0 & 0 & \sin (\theta_G + \lambda_E) \\ -\cos (\theta_G + \lambda_E) & -\sin (\theta_G + \lambda_E) & 0 \end{bmatrix} \mathbf{R}_S \tag{22}
$$

Comparing Eq. (20) with Eqs. (21) and (22) it appears that the observing station's longitude and latitude will both be affected by errors in precession. If a drift on the order of 1/3 m/yr is significant, then the effect of precession should be considered in estimating station coordinates.

References

1. *Explanatory Supplement to the Astronomical Ephemeris and the American Ephemeris and Nautical Almanac.* Her Majesty's Nautical Almanac Office, Her Majesty's Stationery Office, London, 1961.

2. Lieske, J., *Expressions for the Precession Quantities and Their Partial Derivatives*, Technical Report No. 32-1044. Jet Propulsion Laboratory, Pasadena, Calif., 1967.

3. Fricke, W., "Precession and Galactic Rotation from McCormick and Cape Proper Motions in the Systems FK3, N30, FK4," *Astron. J.*, Vol. 72, pp. 642–649, 1967.

4. Fricke, W., "Precession and Galactic Rotation Derived From Fundamental Proper Motions of Distant Stars," *Astron. J.*, Vol. 72, pp. 1368–1379, 1967.

5. Clemence, G., "The System of Astronomical Constants," *Ann. Rev. Astron. Astrophys.*, Vol. 3, pp. 93–111, 1965.

D. Behavior of a Clock Moving Radially in a Centrally Symmetric Gravitational Field,

H. Lass and P. Gottlieb

In a similarly titled paper by R. F. Polishchuk (Ref. 1) the proper time for a test particle moving in a Schwarzchild field under the action of external fields is determined. It is shown that, under certain circumstances, the proper time for the moving object when it returns to its point of departure will exceed the proper time for the object remaining at rest at the point of departure. However, as we will subsequently show, there is a fundamental error in Polishchuk's paper. We will determine, with the proper analysis, that the readings of a moving clock may be less than or may exceed the readings of a stationary clock remaining at the point of departure.

We begin with an analysis of the geodesics (motion of a test particle) associated with the Riemannian metric given by

$$ds^2 = g_{\alpha\beta}\, dx^\alpha\, dx^\beta \tag{1}$$

The geodesics are given by

$$\frac{\delta u^i}{\delta s} = \frac{d^2 x^i}{ds^2} + \Gamma^i_{jk} \frac{dx^j}{ds} \frac{dx^k}{ds} = 0 \tag{2}$$

with $u^i = dx^i/ds$, and $\delta u^i/\delta s$ the intrinsic derivative.

If external forces are applied, the equations of motion are given by

$$\frac{\delta u^i}{\delta s} = F^i \tag{3}$$

with F^i a 4-vector, the external force.

Defining $u_i = g_{ij} u^j$ yields

$$u_i u^i = g_{ij} \frac{dx^i}{ds} \frac{dx^j}{ds} \equiv 1$$

along any path, by virtue of Eq. (1). From Eq. (3) we have

$$u_i \frac{\delta u^i}{\delta s} = \frac{1}{2} \frac{\delta}{\delta s}(u_i u^i) = u_i F^i = 0 \tag{4}$$

so that the components $F^i, i = 1, 2, 3, 4$, are not independent, as assumed by Polishchuk.

Let us now turn to the Schwarzchild line element

$$ds^2 = c^2\left(1 - \frac{2GM}{c^2 r}\right) dt^2 - \left(1 - \frac{2GM}{c^2 r}\right)^{-1} dr^2 - r^2 (d\theta^2 + \sin^2\theta\, d\phi^2) \tag{5}$$

For pure radial motion, $d\theta = d\phi = 0$, and

$$ds^2 = c^2\left(1 - \frac{2GM}{c^2 r}\right) dt^2 - \left(1 - \frac{2GM}{c^2 r}\right)^{-1} dr^2 \tag{6}$$

From Eq. (4) it follows that

$$\left(1 - \frac{2GM}{c^2 r}\right) c \frac{dt}{ds} F_t - \left(1 - \frac{2GM}{c^2 r}\right)^{-1} \frac{dr}{ds} F_r = 0 \tag{7}$$

with $F^1 = F_r, F^4 = F_t$.

Eq. (3), with

$$i = 4, \frac{dx^4}{ds} = c\frac{dt}{ds},$$

becomes

$$c\frac{d^2 t}{ds^2} + \frac{\dfrac{2GM}{c^2 r^2}}{1 - \dfrac{2GM}{c^2 r}} \frac{dr}{ds} c \frac{dt}{ds} = F_t = \frac{\dfrac{dr}{ds} F_r}{\left(1 - \dfrac{2GM}{c^2 r}\right)^2 c \dfrac{dt}{ds}} \tag{8}$$

Now suppose that the test particle is located at $r = r_0$ with $dr/ds = 0$. We apply an external radial force

$$F_r = \frac{F_0}{c^2} + \frac{GM}{c^2 r^2}$$

which is sufficient to overcome gravity, so that the particle begins to accelerate outward ($F_0 > 0, F_0$ a constant).

With this value of F_r, Eq. (8) yields a first integral

$$c^2\left(\frac{dt}{ds}\right)^2 = \frac{2\left(\dfrac{F_0 r}{c^2} - \dfrac{GM}{c^2 r} + A\right)}{\left(1 - \dfrac{2GM}{c^2 r}\right)^2} \tag{9}$$

To find the radial motion one eliminates dt between Eqs. (6) and (9) to obtain

$$\left(\frac{dr}{ds}\right)^2 = \frac{2F_0}{c^2}(r - r_0) \tag{10}$$

with

$$\frac{dr}{ds} = 0 \text{ for } r = r_0.$$

The proper time for the particle to move from r_0 to $r_1 > r_0$ is

$$\tau_{01} = \int \frac{ds}{c} = \frac{1}{(2F_0)^{1/2}} \int_{r_0}^{r_1} \frac{dr}{(r - r_0)^{1/2}} = \left[\frac{2(r_1 - r_0)}{F_0}\right]^{1/2} \tag{11}$$

which is equivalent to the Newtonian time.

Let us now choose r_1 such that if the thrust F_r were removed, the particle would have escape velocity at this point. We note that for a free particle

$$c\left(1 - \frac{2GM}{c^2 r}\right)\frac{dt}{ds} = k = \text{constant} \tag{12}$$

is a first integral. From Eq. (6) we obtain

$$1 = \frac{k^2}{1 - \dfrac{2GM}{c^2 r}} - \frac{1}{1 - \dfrac{2GM}{c^2 r}}\left(\frac{dr}{ds}\right)^2 \tag{13}$$

With $dr/ds = 0$ at $r = \infty$ we obtain $k = 1$, so that

$$\left(\frac{dr}{ds}\right)^2 = \frac{2GM}{c^2 r}$$

At $r = r_1$, Eq. (10) yields

$$F_0 = \frac{GM}{r_1(r_1 - r_0)} \tag{14}$$

which yields the value of F_0 for a given r_1 in order that the test particle reach r_1 with escape velocity.

The proper time for the particle to coast from r_1 to $r_2 > r_1$ is

$$\tau_{12} = \int \frac{ds}{c} = \frac{1}{(2GM)^{1/2}} \int_{r_1}^{r_2} (r)^{1/2}\, dr = \frac{2}{3(2GM)^{1/2}}(r_2^{3/2} - r_1^{3/2}) \tag{15}$$

At r_2 we apply a radial thrust given by

$$F_r = -\frac{F_1}{c^2} + \frac{GM}{c^2 r^2}$$

until the particle comes to rest at $r_3 > r_2$. As in the previous analysis it is quite simple to show that the proper time for the particle to travel from r_2 to r_3 is

$$\tau_{23} = \left[\frac{2(r_3 - r_2)}{F_1}\right]^{1/2} \tag{16}$$

with

$$F_1 = \frac{GM}{r_2(r_3 - r_2)}$$

The return journey of the test particle is accomplished in the same fashion as its outward journey. The reading of the moving clock for the entire journey is given by

$$\tau = 2\left[\left(\frac{2r_1}{GM}\right)^{1/2}(r_1 - r_0) + \frac{1}{3}\left(\frac{2}{GM}\right)^{1/2}(r_2^{3/2} - r_1^{3/2}) + \left(\frac{2r_2}{GM}\right)^{1/2}(r_3 - r_2)\right] \tag{17}$$

In order to compute the proper time for the journey as viewed by the stationary observer, we must compute the coordinate time T for the journey. The proper time will be given by

$$T' = \left(1 - \frac{2GM}{c^2 r_0}\right)^{1/2} T \tag{18}$$

To compute the coordinate time for the journey from r_0 to r_1 we eliminate ds between Eqs. (6) and (10). This yields

$$dt = \frac{\left(1 + \dfrac{1}{c^2}\left[2F_0(r - r_0) - \dfrac{2GM}{r}\right]\right)^{1/2}}{\left[2F_0(r - r_0)\left(1 - \dfrac{2GM}{c^2 r}\right)\right]^{1/2}}\, dr \tag{19}$$

Neglecting terms of the order $1/c^4$ and higher yields

$$dt = \frac{1}{(2F_0)^{1/2}}\left\{(r - r_0)^{-1/2} + \frac{1}{c^2} \times \left[F_0(r - r_0)^{1/2} + \frac{GM}{r}(r - r_0)^{-1/2}\right]\right\} dr \tag{20}$$

An integration from r_0 to r_1 yields the coordinate time

$$T_{01} = \left(\frac{2r_1}{GM}\right)^{1/2}(r_1 - r_0) + \frac{1}{c^2} \times \left[\frac{1}{3}\left(\frac{2GM}{r_1}\right)^{1/2}(r_1 - r_0) + \left(\frac{2GM\, r_1 (r_1 - r_0)}{r_0}\right)^{1/2} \tan^{-1}\left(\frac{r_1 - r_0}{r_0}\right)^{1/2}\right] \tag{21}$$

We note for $c = \infty$, that $T_{01} = \tau_{01}$, as expected.

During the coast period from r_1 to r_2 we have

$$\left(\frac{dr}{ds}\right)^2 = \frac{2GM}{c^2 r}$$

Eliminating ds^2 from Eq. (6) yields

$$dt = \frac{1}{(2GM)^{1/2}} \frac{(r)^{1/2}\, dr}{1 - \dfrac{2GM}{c^2 r}} \approx \frac{1}{(2GM)^{1/2}} (r)^{1/2} \left(1 + \frac{2GM}{c^2 r}\right) dr \tag{22}$$

A simple integration yields the coordinate time for this part of the journey, given by

$$T_{12} = \frac{1}{3}\left(\frac{2}{GM}\right)^{1/2} (r_2^{3/2} - r_1^{3/2}) + \frac{2}{c^2}(2GM)^{1/2}((r_2)^{1/2} - (r_1)^{1/2}) \tag{23}$$

Neglecting $1/c^4$ terms, etc., the coordinate time during the deceleration period from r_2 to r_3, can be shown to be

$$T_{23} = \left(\frac{2r_2}{GM}\right)^{1/2}(r_3 - r_2) + \frac{1}{3c^2}\left(\frac{2GM}{r_2}\right)^{1/2}(r_3 - r_2) + \frac{1}{c^2}\left[\frac{GMr_2(r_3 - r_2)}{2r_3}\right]^{1/2} \ln\frac{(r_3)^{1/2} + (r_3 - r_2)^{1/2}}{(r_3)^{1/2} - (r_3 - r_2)^{1/2}} \tag{24}$$

The total coordinate time for the trip is

$$T = 2(T_{01} + T_{12} + T_{23}) \tag{25}$$

and the proper time for the trip as noted by the stationary observer is

$$T' = T\left(1 - \frac{2GM}{c^2 r_0}\right)^{1/2} \approx T\left(1 - \frac{GM}{c^2 r_0}\right) \tag{26}$$

It is then a simple matter to show within the order of $1/c^2$ terms that

$$\begin{aligned} T' - \tau = \frac{2}{c^2}\Bigg\{ & (2GM)^{1/2}(r_1 - r_0)\left(\frac{r_0 - 3r_1}{3r_0 (r_1)^{1/2}}\right) \\ & + (2GM)^{1/2}(r_3 - r_2)\left(\frac{r_0 - 3r_2}{3r_0 (r_2)^{1/2}}\right) \\ & + (2GM)^{1/2}[(r_2)^{1/2} - (r_1)^{1/2}] \\ & \times \left[2 - \frac{1}{3r_0}(r_1 + r_2 + (r_1 r_2)^{1/2})\right] \\ & + \left[\frac{2GMr_1(r_1 - r_0)}{r_0}\right]^{1/2} \tan^{-1}\left(\frac{r_1 - r_0}{r_0}\right)^{1/2} \\ & + \left[\frac{GMr_2(r_3 - r_2)}{2r_3}\right]^{1/2} \ln\frac{(r_3)^{1/2} + (r_3 - r_2)^{1/2}}{(r_3)^{1/2} - (r_3 - r_2)^{1/2}}\Bigg\} \end{aligned} \tag{27}$$

The last expression in Eq. (27) shows that for $r_3 >> r_2$ one has $T' > \tau$, and the reading of the moving clock will be less than the reading of the stationary clock.

On the other hand, if $r_3 \approx r_2$ and $r_1 \approx r_0$, the middle term of Eq. (27) shows that $T' < \tau$ for $r_2 >> r_1 > r_0$. Thus, if the coasting period is of long duration compared to the acceleration periods, the reading of the moving clock will be greater than the reading of the stationary clock. In order that one can coast for a considerable distance one must reach r_1 at escape velocity. The long coasting period as well as the red shift for the stationary observer yields $T' < \tau$, a result opposite to that of the special relativity effect wherein $T' > \tau$.

Reference

1. Polishchuk, R. F., "Behavior of a Clock Moving in a Centrally Symmetric Gravitational Field," *Sov. Astron.–AJ*, Vol. II, No. 5, Mar.–Apr. 1968.

E. A Simulated Least Squares Solution for Parameters of the *Mariner* Mars 1969 Encounter Orbit, *J. D. Anderson*

The purpose of this article is to establish the need for range data from the viewpoint of the *Mariner* Mars 1969 celestial mechanics experiment. This has been done before (SPS 37-44, Vol. IV, pp. 4–8 and SPS 37-47, Vol. III, pp. 1–7) for data in both the cruise and encounter phases of the mission. The basic conclusion of these earlier studies is that range data aid in the improvement of the mass and geocentric position of Mars, particularly when the cooling gas venting from the infrared spectrometer is taken into account.

Recently a shorter interval of data during the encounter phase of the mission has been simulated (from $E - 3.5$ days to $E + 3.5$ days), and the effect of adding or deleting Mars DSS range data from a least squares encounter solution has been studied. Doppler data have been simulated at a 15-min sample interval with an accuracy of ± 0.395 mm/s and have been assumed available on a continuous basis except for a period of about 32½ min during earth occultation. Results of this recent study are given in Table 1.

Table 1. Comparison of standard errors for simulated *Mariner* Mars 1969 encounter solutions with and without range data

Parameter	*A priori* error	Range and doppler	Doppler only
X, km	10^{6}	3.49	4.21
Y, km	10^{6}	8.31	17.00
Z, km	10^{6}	19.32	24.29
DX, mm/s	10^{6}	11.1	13.5
DY, mm/s	10^{6}	26.2	33.5
DZ, mm/s	10^{6}	26.2	33.5
$r_{\oplus♂}$, m	10^{7}	27.6	8014
$\dot{r}_{\oplus♂}$, mm/s	10^{3}	68.2	92.6
$m_{♂}$, ppm	1960	27.1	37.3
R_{51}, m	1.0	0.46	0.49
λ_{51}, deg	30×10^{-6}	5.6×10^{-6}	8.4×10^{-6}
R_{12}, m	1.0	0.67	0.68
λ_{12}, deg	30×10^{-6}	6.3×10^{-6}	9.1×10^{-6}

The parameters of the solution are given in column 1 in terms of the geocentric position and velocity (X, Y, Z, DX, DY, DZ) of the spacecraft at $E - 3½$ days, the geocentric range $r_{\oplus♂}$ and range rate $\dot{r}_{\oplus♂}$ of the center of mass of Mars, the mass of Mars m (error units are in parts per million), and the geocentric radii and longitudes of Johannesburg and Echo DSSs which were used in the simulation of the doppler data. The assumed *a priori* errors on these parameters are given in column 2, and the standard errors from a doppler-only solution are given in column 4. In column 3 the effect on the standard errors from the addition of Mars DSS range data is given. As with the doppler data, range data were sampled once every 15 min and were assumed to have a standard error of 100 m in one-way range.

Results obtained from Table 1 are qualitatively similar to the earlier studies. Perhaps the most important conclusion is that range data are absolutely necessary to determine the geocentric distance to Mars at planetary encounter. Studies by Curkendall and McReynolds (Ref. 1) are consistent with this conclusion. By looking at Fig. 8 in their paper, it can be concluded that at the *Mariner* Mars 1969 encounter the geometry is not favorable for determining range to the spacecraft from doppler data alone. A major objective of the celestial mechanics experiment is to obtain a good range measurement at encounter and then to compare it with anticipated radar bounce measurements from Mars to determine the physical size of the planet.

Reference

1. Curkendall, D. W., and McReynolds, S. R., *A Simplified Approach for Determining the Information Content and Critical Error Sources of Earth-Based Radio Tracking Data*, AAS Paper 68-112, Sept. 3–5, 1968.

F. Computational Accuracy of Square-Root Filtering, *P. Dyer and S. R. McReynolds*

1. Introduction

Two approaches to square root filtering have emerged recently. One, an approach formulated by Potter (Ref. 1), is based on the computation of the square root of *the covariance matrix*. The other approach, suggested by Businger and Golub (Ref. 2), relies on the computation of the square root of *the information matrix*, and involves the application of Householder transformations (Ref. 3).

Both algorithms were described for systems with uncorrelated measurements and without process noise, although Bellantoni and Dodge (Ref. 4) and Andrew (Ref. 5) have extended Potter's algorithm to incorporate correlated measurements. Recently the authors extended both algorithms to include the effects of process noise.

The classical approach to sequential filtering for systems with process noise is due to Kalman (Ref. 6). Unfortunately, the computation of the Kalman filter is vulnerable to numerical errors, which often results in a computed covariance matrix which is nonpositive. The main advantage of the square root algorithms is that a greater precision is retained. Thus the range of effective observability is extended; that is, more poorly observed variables may be estimated. This property will be illustrated in an example, the estimation of the position of a space probe from doppler measurements. It is also possible to reformulate the basic Kalman filter algorithm to reduce numerical errors (Ref. 7); however, the square-root filters are superior.

2. The Problem

Consider a system described by the transition equations

$$x(k+1) = F(x)\,x(k) + G(k)\,w(k) \qquad k = 1, 2, \cdots, N \tag{1}$$

where

$$x(k) = [x_1(k), x_2(k), \cdots, x_n(k)]$$

is the state of the system, and

$$w(k) = [w_1(k), w_2(k), \cdots, w_n(k)]$$

is the process noise at the kth epoch. The matrices F and G are $n \times n$. The measurements at the kth epoch are denoted by

$$z(k) = [z_1(k), z_2(k), \cdots, z_r(k)]$$

where

$$z(k) = H(k)\,x(k) + Q(k)\,v(k) \qquad k = 1, 2, \cdots, N \tag{2}$$

The measurement noise is denoted by

$$v(k) = [v_1(k), v_2(k), \cdots, v_r(k)]$$

The matrix H is $r \times n$ and Q is $r \times r$. It is assumed that *all* the measurements are noisy, i.e., the matrix Q has full rank.

The components of w and v are assumed to be statistically independent and gaussian, with zero means and unit variances. This assumption is not restrictive, because any set of correlated gaussian random variables may be linearly transformed to a new set of independent gaussian random variables. One technique which effects this transformation is as follows. Let $w(k)$ denote correlated process noise with covariance $C(k)$. Now employing the Cholesky square root algorithm (Ref. 8) a matrix $D(k)$ is found such that

$$C(k) = D(k)\,D(k)^T$$

Equation (1) may now be written

$$x(k+1) = F(k)\,x(k) + G(k)\,D(k)\,w(k)$$

where the components of $w(k)$ are independent random parameters with zero mean and unit covariance.

The problem of estimating $x(k)$ is equivalent to minimizing $J(k)$, where,

$$J(k) = \sum_{i=1}^{k} \{\|v(i)\|^2 + \|w(i)\|^2\} + \|x(1) - \bar{x}(1)\|^2\,\Lambda^{-1}(1) \tag{3}$$

subject to the constraints of Eqs. (1) and (2). In Eq. (3)

$$\bar{x}(1) = \textit{a priori} \text{ mean of } x(1)$$

$$\Lambda(1) = \textit{a priori} \text{ covariance of } x(1).$$

3. Square-Root Filters

Let $J_{opt}(k)$ denote the minimum return function[3] for this problem expressed in terms of $x(k)$. Then

$$J_{opt}(k) = \|x(k) - \bar{x}(k)\|^2\,\Lambda^{-1}(k) + r^2(k) \tag{4}$$

Here

$$\bar{x}(k) = \text{the conditional mean of } x(k)$$

and

$$\Lambda(k) = \text{the conditional covariance}$$

$$r^2(k) = \text{sum of the squares of the residuals}$$

The solution to the filtering problem is provided once $J_{opt}(k)$ is computed.

The Kalman filter computes $J_{opt}(k)$ by computing $\Lambda(k)$ and $\bar{x}(k)$. However, the square root filter based on the Householder transformation computes $R(k)$ and $d(k)$ where

$$\begin{aligned} R(k) &= \Lambda^{-1/2}(k) \\ d(k) &= \Lambda^{-1/2}(k)\,\bar{x}(k) \end{aligned} \tag{5}$$

In terms of $R(k)$ and $d(k)$, the return $J_{opt}(k)$ is given by

$$J_{opt}(k) = \|R(k)\,x(k) - d(k)\|^2 + r^2(k) \tag{6}$$

Clearly $\bar{x}(k)$ and $\Lambda(k)$ are given by

$$\begin{aligned} \bar{x}(k) &= R^{-1}(k)\,d(k) \\ \Lambda(k) &= R^{-1}(k)\,R^{-1}(k)^T \end{aligned} \tag{7}$$

The Potter square root filter computes $\bar{x}(k)$ and $S(k)$, where

$$S(k) = \Lambda(k)^{1/2}$$

[3]See Ref. 9 for the formulation of sequential estimation in terms of dynamic programming.

i.e., $\Lambda(k) = S(k)\,S(k)^T$. Thus

$$S(k) = (R^T(k))^{-1}$$

a. Application of the algorithm. While it is very easy to illustrate the numerical advantages of the procedure with a simple example, it is not so straightforward with a practical example. This is because in such a case, the true solution is generally unknown. We will, therefore, first consider a simple example which may be solved with a least-squares approach.

Example 1[4]

Consider a system of two unknowns $X(1)$ and $X(2)$ and three measurements $Z(1)$, $Z(2)$, and $Z(3)$. The relevant measurement matrix H, is chosen to be

$$H = \begin{bmatrix} 1 & 1 \\ 1 & 1 \\ 1 & 1+e \end{bmatrix} \tag{8}$$

and the noise matrix Q equals the unit matrix. By varying the parameter e the conditioning of the matrix H^TH may be controlled. Now if the measurements are chosen to be $[1, 1, 1]$, the solution is,

$$\begin{aligned} X(1) &= 1 \\ X(2) &= 0 \end{aligned} \tag{9}$$

The solutions obtained via a double-precision least squares program are compared with that given by the Householder square root algorithm in Table 2,[5] which vividly demonstrates the inaccuracies of the least squares approach. With the new algorithm, a correct solution is obtained until $e = 10^{-11}$. One of the features of the program is that a solution of minimum euclidean length is generated when the system has less than full rank. This property is illustrated by the last rows of the table.

[4]This example was shown to the authors by R. Hanson.

[5]The Potter algorithm could not be used here as there was no *a priori* information.

Example 2

The second example is concerned with the orbit determination of a space probe using range-rate measurements. It is characterized by a great disparity in the observability of different components of the state and hence is an ideal problem with which to illustrate the properties of the various estimation algorithms.

The coordinate system used is shown in Fig. 8 where X_p, Y_p, Z_p, $\dot{X}_p$, $\dot{Y}_p$, and $\dot{Z}_p$ represent the position and

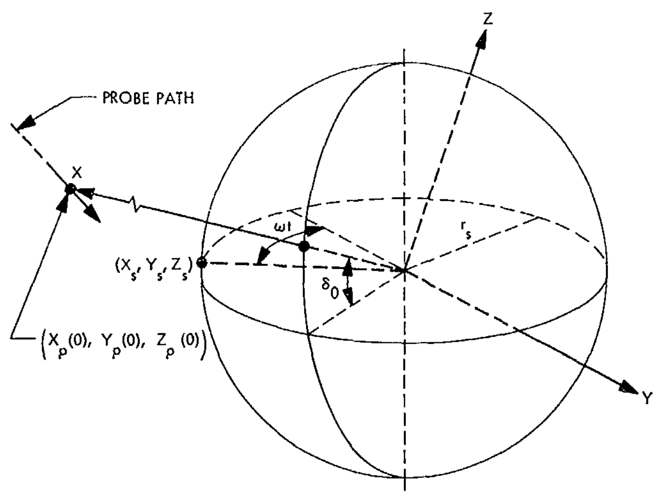

$X_s = r_s \sin \omega t \cos \delta_0$ $\qquad$ $\dot{X}_s = \omega r_s \cos \omega t \cos \delta_0$

$Y_s = -r_s \cos \omega t$ $\qquad$ $\dot{Y}_s = \omega r_s \sin \omega t$

$Z_s = -r_s \sin \omega t \sin \delta_0$ $\qquad$ $\dot{Z}_s = \omega r_s \cos \omega t \sin \delta_0$

WHERE $\delta_0 = 0.34$, AND $r_s = 5212$

Fig. 8. Coordinate system

Table 2. Relative accuracy, Example 1

Value	Least squares		Orthogonal	Transformation
e	X (1)	X (2)	X (1)	X (2)
10^{-1}	1.000000000000000	−0.0000000000000568	0.9999999999999995	0.0000000000000004
10^{-3}	1.000000000010914	−0.0000000000109139	1.000000000000000	0.0000000000000000
10^{-4}	1.000000000465661	−0.0000000009313226	1.000000000000000	0.0000000000000000
10^{-5}	1.000007629394531	−0.0000038146972656	0.9999999999999997	0.0000000000000002
10^{-7}	1.062500000000000	−0.0625000000000000	0.9999999999999996	0.0000000000000003
10^{-9}	1.000000000000000	−1.000000000000000	0.9999999999999996	0.0000000000000004
10^{-11}	1.0	−1.0	0.9999999999999997	0.0000000000000002
10^{-15}	1.0	−0.5	0.4999999999999995	0.4999999999999995

velocity of the probe, and X_s, Y_s, Z_s, $\dot{X}_s$, $\dot{Y}_s$, and $\dot{Z}_s$ denote the position and velocity of the tracking station. The doppler, or range-rate measurement, ρ is a measure of the velocity along the line from the tracking station to the space probe, i.e.,

$$\dot{\rho} = \frac{\mathbf{X}}{|\mathbf{X}|} \cdot \mathbf{V}$$

where $\mathbf{X}$ and $\mathbf{V}$ are the vectors.

$$\mathbf{X} = \begin{bmatrix} X_p - X_s \\ Y_p - Y_s \\ Z_p - Z_s \end{bmatrix} \qquad \mathbf{V} = \begin{bmatrix} \dot{X}_p - \dot{X}_s \\ \dot{Y}_p - \dot{Y}_s \\ \dot{Z}_p - \dot{Z}_s \end{bmatrix}$$

Thus the required partial derivatives relating to the state of the probe and the data are given by

$$\frac{\partial \dot{\rho}}{\partial V(i)} = \frac{X(i)}{r} \qquad i = 1, 2, 3$$

$$\frac{\partial \dot{\rho}}{X(i)} = \frac{V(i)}{r} - \frac{u\,X(i)}{r^2} \qquad i = 1, 2, 3$$

where the radius

$$r = [X(1)^2 + X(2)^2 + X(3)^2]^{1/2}$$

and the velocity along the radius

$$u = [X(1)\,V(1) + X(2)\,V(2) + X(3)\,V(3)]/r$$

Simple straight-line motion relative to the earth's center was assumed for the probe, i.e.,

$$\ddot{X}_p = 0$$

$$\ddot{Y}_p = 0$$

$$\ddot{Z}_p = 0$$

where the initial state was assumed to be

$$X_p(1) = 10^8\,\mathrm{km}$$

$$X_p(2) = X_p(3) = 0$$

$$V_p(1) = V_p(3) = 0$$

$$V_p(2) = 10\,\mathrm{km/s}$$

It was also assumed that the probe was tracked for two 12-h passes with a 12-h break in the middle while the tracking station was hidden from the probe. Measurements were taken once a minute. The numerical conditioning of the system was adjusted by the choice of the *a priori* covariance; increasing the covariance worsened the conditioning. The measurement noise was assumed to have a variance of $10^{-12}\,(\mathrm{km/s})^2$.

First several cases were chosen to compare the accuracy of the various filters *without* process noise. Kalman, Angstron-Koepcke-Tung, Potter, and Householder filters were tried with various *a priori* matrices. The *a priori* matrices were unit matrices multiplied by 10^8, 10^{12}, and 10^{16}. One final run was made, with no *a priori* information, with the orthogonal filter. The diagonal elements of the final covariance matrices are shown in Table 3.

As can be seen, the two square root filters give essentially the same results. The normal Kalman filter is not nearly as accurate as the Angstrom-Koepcke-Tung filter in the first case, although both fail as *a priori* information decreases.

Next process noise was added to the system. The *a priori* covariance was taken as 10^{12} times the unit matrix, and the covariance of the process noise was taken as

$$10^{-8} \times I \quad (\mathrm{km/sec^2})^2$$

and

$$10^{-10} \times I \quad (\mathrm{km/sec^2})^2$$

Diagonal elements of the final covariance matrices are shown in Table 4 for the square root filters. The filters give essentially equivalent results. The same cases were tried with the other filters and, although positive diagonals were obtained in the first case, the numbers were not accurate to even one significant figure.

Clearly, if the system is badly conditioned, the square root filters give superior results. No marked difference was found between the two square root filters. The orthogonal filter was somewhat more complex to program but could handle problems with *no a priori* information. Furthermore, rank-deficient solutions could easily be obtained. There was little difference in computer time between the various filters.

References

1. Battin, R., *Astronautical Guidance*, p. 339, McGraw Hill Book Co., Inc., New York, 1964.
2. Businger, P., and Golub, G., "Linear Least Squares Solution by Householder Transformation," *Numer. Math.*, Vol. 7, pp. 269–275, 1968.
3. Householder, A. S., *The Theory of Matrices in Numerical Analysis*, Chap. 5, Blaisdell Pub. Co., New York, 1964.
4. Bellatoni, J. F., and Dodge, K. W., "A Square Root Formulation of the Kalman-Schmidt Filter," *AIAA Journal*, Vol. 5, No. 7, pp. 1309–1314, July 1967.
5. Andrews, A., "A Square Root Formulation of the Kalman Covariance Equations," *AIAA Journal*, Vol. 6, No. 6, pp. 1165–1166, June 1968.
6. Kalman, R. E., "A New Approach to Linear Filtering and Prediction Problems," J. Basic Engineering 82 D, pp. 35–45, 1960.
7. Astrom, K. J., Koepcke, R. W., and Tung, F., "On the Control of Linear Discrete Dynamic Systems With Quadratic Loss," Report RJ 222, IBM Research Laboratory, San Jose, Calif., 1962.
8. Faddeeva, V. N., "Computational Methods of Linear Algebra," pp. 81–85, Dover Publications, 1959.
9. Cox, H. C., "Estimation of State Variables via Dynamic Programming," Proceedings of 1964 Joint Automatic Control Conference, pp. 376–381, 1964.

Table 3. Comparison of sequential filters

A priori covariances	Filter	$P(1,1)\times 10^{8}$	$P(2,2)\times 10^{1}$	$P(3,3)\times 10^{1}$	$P(4,4)\times 10^{-11}$	$P(5,5)\times 10^{-7}$	$P(6,6)\times 10^{-6}$
10^{8}	a	0.4048820	0.4166330	0.2008347	0.7749189	0.9823329	0.3004011
	b	0.4033534	0.4156932	0.1907584	0.7751610	0.9786459	0.2941951
	c	0.4033529	0.4156927	0.1907590	0.7751611	0.9786449	0.2941994
	d	0.4033529	0.4156928	0.1907590	0.7751611	0.9786449	0.2941994
10^{12}	a			Negative diagonals			
	b			Negative diagonals			
	c	0.6760298	0.6705581	0.1967947	1.052819	1.640169	0.2942901
	d	0.6760305	0.6705590	0.1967947	1.052820	1.640170	0.2942902
10^{16}	a			Negative diagonals			
	b			Negative diagonals			
	c	0.6760214	0.6705354	0.1967956	1.052758	1.640149	0.2942843
	d	0.6760762	0.6706017	0.1967957	1.052867	1.640281	0.2942902
∞	d	0.6760762	0.6706017	0.1967957	1.052867	1.640281	0.2942902

[a] Kalman.
[b] Angstrom–Koepcke–Tung.
[c] Potter.
[d] Householder.

Table 4. Estimation with process noise

Noise, $(km/s^2)^2$	Filter	$P(1,1)\times 10^{10}$	$P(2,2)\times 10^{6}$	$P(3,3)\times 10^{6}$	$P(4,4)\times 10^{-9}$	$P(5,5)\times 10^{-4}$	$P(6,6)\times 10^{-4}$
10^{-8}	Potter	0.4281827	0.4341234	0.2948340	0.7594377	0.1066931	0.7257993
	Householder	0.4281825	0.4341231	0.2948340	0.7594372	0.1066931	0.7257993
		$\times 10^{8}$	$\times 10^{4}$	$\times 10^{4}$	$\times 10^{-10}$	$\times 10^{-6}$	$\times 10^{-6}$
10^{-10}	Potter	0.6811936	0.6758202	0.2016849	0.1061979	0.1652994	0.3035435
	Householder	0.6811929	0.6758192	0.2016848	0.1061977	0.1652992	0.3035434

II. Systems Analysis

SYSTEMS DIVISION

A. ASTRAL: Optimized Low-Thrust Trajectories Using Approximate Closed-Form Solutions to the Equations of Motion, *W. Stavro and D. J. Alderson*

1. Introduction

Investigators performing analysis of low-thrust trajectories have generally used two approaches to the problem. These approaches are not alternatives to one another, but are independent and justifiable pursuits. The first approach, which is also historically the first, was to attempt to solve the equations of motion of the spacecraft analytically and thus determine its path. This involved the solution of nonlinear differential equations using generally some kind of perturbation scheme. The second approach was to solve the boundary-value optimization problem (where the boundary values are the initial and final position and velocity of the spacecraft for a specified mission) and determine the optimal thrust programs to maximize certain mission parameters. This generally involved the use of the calculus of variations and quite extensive numerical techniques.

Basically, the engineering purpose of studying low-thrust trajectories is to develop a tool to be used in the design and planning of space exploration missions. From this point of view, researchers who followed the second approach (optimization) may be considered to be those who concerned themselves more intimately with the real problem of mission design. However, it must be realized that analysis using the first approach has two great advantages. In the first place, an analytic investigation into the basic equations of motion gives great insight into the general behavior of such trajectories, as for example, the determination of the behavior of the osculating orbital elements. Secondly, the computing time needed to obtain numerical results from the approximate closed-form solutions is appreciably less than the time needed to perform numerical integrations of the equations of motion, thus a computer program which gives approximate results but is simple and fast would be an extremely useful tool for the design of low-thrust trajectories if the approximate results are accurate enough.

A survey of the literature on low-thrust investigations shows that as these approaches were further developed and expanded they became almost completely independent fields of study. For example, intensive work in low-thrust mission optimization made no use of closed-form approximate solutions of the equations of motion, and similarly investigators who developed approximate solutions made no attempt to use these in mission analysis studies.

ASTRAL is the first attempt to combine both these fields of endeavor in order to obtain a useful tool to be utilized in low-thrust mission studies. More specifically, ASTRAL will use an approximate closed-form solution to the differential equations of motion, together with an optimization scheme, to obtain a program that optimizes various mission parameters to maximize a low-thrust payload.

The purpose of this article is to broadly present a description of ASTRAL and to explain the overall structure of the program and its content. An attempt was made to stay away from program specifics, such as input and output format and actual form of the program. These will be published after the program is checked out and is in a working condition.

2. Trajectory Analysis

Numerous attempts have been made to solve the differential equations of motion of a spacecraft under the influence of low thrust. These studies ranged in complexity from very simple approximations to very sophisticated perturbation schemes. The most recent method used to solve these nonlinear equations, which also gave the best results, is the two-variable asymptotic expansion method. This method was especially suitable because of the appearance of two time scales (slow time associated with the changing orbital elements, and fast time associated with the motion of the spacecraft) as well as the small parameter ϵ, which is the ratio of thrust acceleration to gravitational acceleration. Shi and Eckstein (Ref. 1) used this method to solve the equations of motion of a spacecraft under the influence of constant-thrust acceleration, i.e., approximately a nuclear–electric propulsion system. All other investigators before them had also limited their analysis to constant thrust or constant-thrust acceleration. However, the mission studies presently under serious consideration for outer planet exploration in the 1970s have solar–electric propulsion systems. For this system, the magnitude of the thrust is a function of the distance to the sun since the solar power decreases as the distance to the sun increases.

Wesseling (Ref. 2) considers the case where the thrust acceleration varies as the inverse of the square of the distance to the sun in a heliocentric trajectory. He uses the two-variable asymptotic expansion procedure and obtains the first three terms of the asymptotic series. One of the very interesting results he obtained for such a thrust behavior is that the eccentricity of the osculating conic increases, whereas it had been found that for constant-thrust acceleration it decreases. This exhibits the fact that the general behavior of the trajectory (such as the variation of the elements) seemed to depend on the behavior of the thrust acceleration. Recent studies on a solar–electric power plant show a variation of thrust acceleration proportional to the inverse of the distance to the sun raised to a power of approximately 1.4. Possible improvements to Wesseling's solution to incorporate this effect are discussed in Subsection 6 of this article.

ASTRAL was initiated here with the purpose of being a level-1 computer program to be used for solar–electric mission studies. A level-1 program is one which is used in generating the bulk of the ideal performance information, and as such must be capable of optimization of trajectory and spacecraft parameters. The approach used is the coupling of Wesseling's solutions with an optimization scheme.

3. PATH Subroutine

The subroutine in the ASTRAL program which calculates the trajectory (i.e., where Wesseling's solutions are programmed) is called PATH.

Wesseling's analysis makes two important assumptions. First, since the method uses a perturbation scheme on ϵ, it is valid only for small values of that parameter, i.e., low thrust. Of course, the smaller the value of ϵ the closer his solution approximates a numerical integration, if everything else is held constant. Secondly, in order to obtain higher-order terms, the assumption of small eccentricity (same order of magnitude as ϵ) had to be made. Other conditions are that thrust acceleration varied as $1/r^2$ (where r is the distance to the sun) and that its direction is arbitrary but fixed. In checking PATH out, an attempt was made to determine how sensitive the solutions are to various values of eccentricity and ϵ.

Wesseling had v ' ' two programs on the 1620 computer: (1) AS .. , which contained his approximate solutions, and NUTRAL, which was a numerical integration of the equations of motion to which he compared some of his results. The same process was repeated for the 7094 computer; both Wesseling's results and a numerical integration were programmed. The first step in checking PATH out was to compare it to the 1620 computer version. Once this was done, the main effort became to determine how well the asymptotic solution approximated the numerical integration of the equations for different values of eccentricity and ϵ.

Figures 1a, 1b, and 1c show two-dimensional trajectories for an ϵ of 0.1: Fig. 1a for an initially circular orbit, Figs. 1b and 1c for initial eccentricities e_0 of 0.1 and 0.5. These and other test cases shown here were run for a thrust pointing at an angle of attack of 45 deg [the angle $\eta = 1/(2)^{1/2}$]. Two plots are shown on each of the graphs: one showing Wesseling's solution, the other showing the numerical integration. Figures 1a and 1b give excellent approximations to the numerical integration, whereas Fig. 1c gives intolerable errors. Figure 1d is the same as

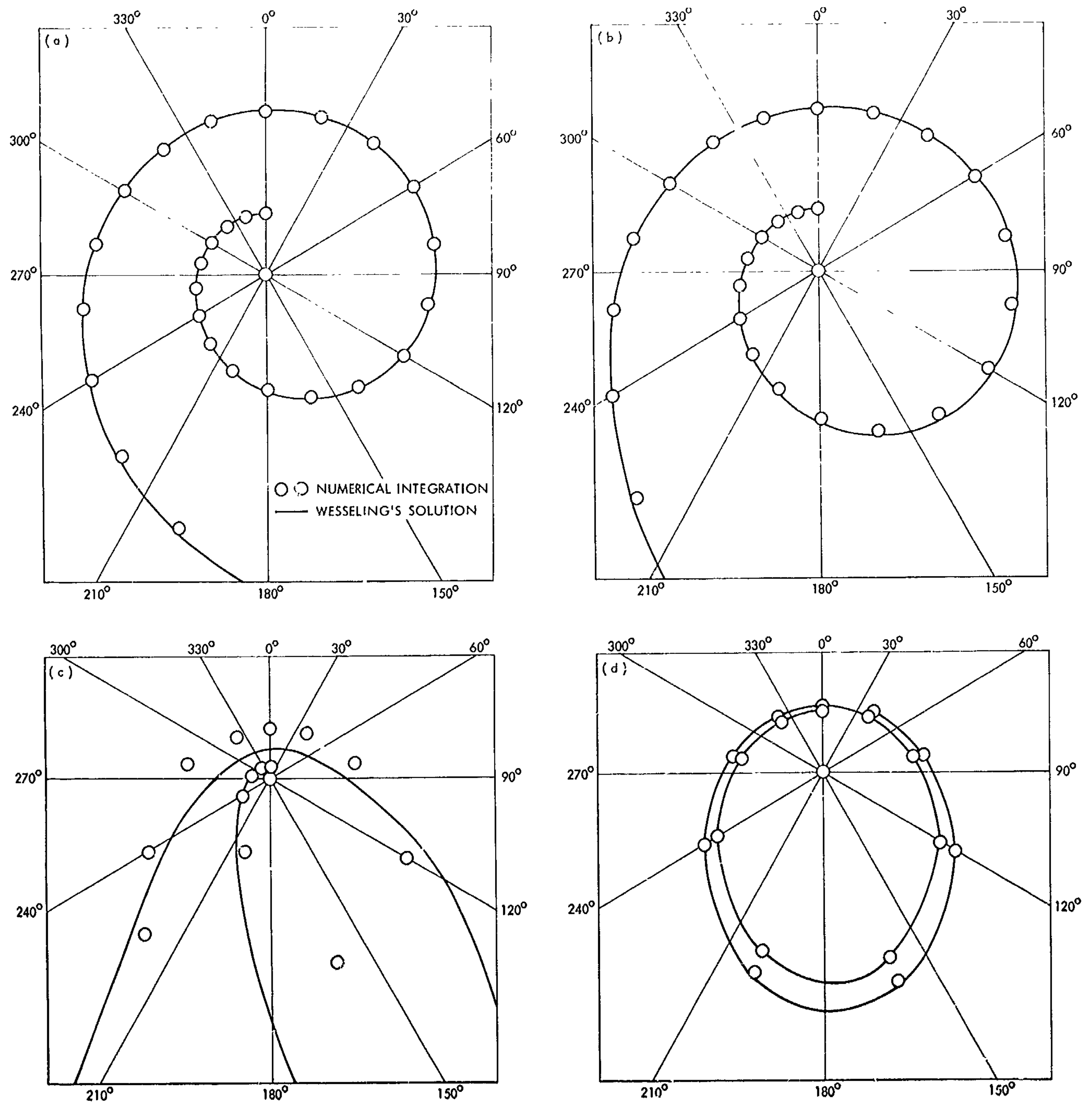

Fig. 1. Two-dimensional trajectories: (a) $e_0 = 0$, $\epsilon = 0.1$; (b) $e_0 = 0.1$, $\epsilon = 0.1$; (c) $e_0 = 0.5$, $\epsilon = 0.1$; (d) $e_0 = 0.5$, $\epsilon = 0.01$

Fig. 1c, except for an ϵ of 0.01, and yields a very good approximation. By studying Figs. 1a and 1d, the following conclusions may be reached:

(1) Excellent approximations are obtained when the initial eccentricity and ϵ are of the order of 0.1 or smaller.

(2) For cases of high eccentricity (about 0.5), the ϵ must be decreased to about 0.01 to obtain good results. This seems to contradict Wesseling's assumption that initial eccentricity has to be of the same order of magnitude as ϵ.

Figure 2 shows time plots for $\epsilon = 0.1$ and initial eccentricities of 0 and 0.1. From these plots, we note that excellent approximations are obtained for about the first half revolution, after which the error increases tremendously, especially for the 0.1 initial eccentricity case. An attempt will be made to investigate these results in order to improve the latter approximations.

Many other runs were made and checked, and, in general, it is concluded that PATH now gives very good approximations to the trajectory of a low-thrust spacecraft whose thrust varies as $1/r^2$, when the initial eccentricity and ϵ are small; and for higher eccentricities, results are still good if ϵ is small enough.

4. Optimization Method

In general, a function-maximizing or optimization method involves the use of a set of one or more points in a parameter space. These points may be restricted to lie within a certain portion of the parameter space, or such constraints may be absent. In either case, the positions and function values, and possibly also function derivative values, of the point or points in the set are used to produce a new point set for further investigation. The resulting sequence of point sets hopefully converges upon the desired optimal location in the parameter space, thus maximizing the given function, subject to the specified constraints if there are any.

In the case under consideration, the partial derivatives of the spacecraft payload with respect to the trajectory parameters cannot be generated in a more efficient manner than by numerical differences, so methods directly using function derivative values are unlikely to be useful. Further, the problem is extensively involved with constraints of all kinds, including some that produce considerable difficulties for methods that make even indirect use of function derivatives. As opposed to these gradient methods, there are the direct search methods.

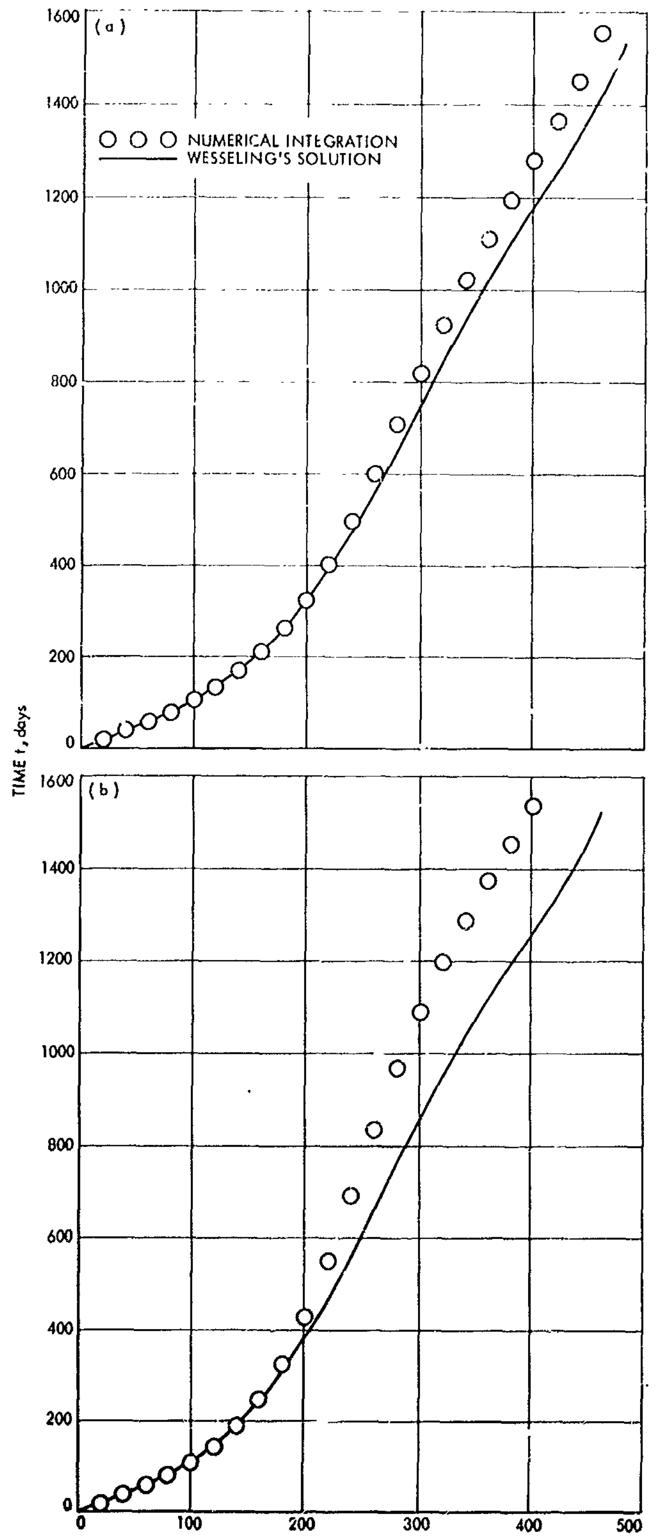

Fig. 2. Time plots: (a) $e_0 = 0$, $\epsilon = 0.1$; (b) $e_0 = 0.1$, $\epsilon = 0.1$

The most effective of these is Box's "complex" method (Ref. 3), and this has been adopted as the basic optimization method in the ASTRAL program.

Maximizing a function of a single variable is qualitatively as well as quantitatively easier than performing the same task with two or more variables. As a result, many multidimensional optimizing methods act by selecting an appropriate one-dimensional subspace of the parameter space and applying a suboptimization process to it. Thus, gradient methods often investigate the line through the point under consideration along which the function is changing most rapidly at the point—the line defined by the gradient vector of the function at the point. The complex method also uses this dimensional reduction technique, though without reference to derivatives. If the parameter space to be dealt with has n dimensions, $n + 1$ or more points in the space are placed in a set. These points form the vertices of a polytope or complex, the n-dimensional equivalent of a polygon or polyhedron.

The one-dimensional subspace chosen for further inspection is that connecting one of the points in the set with the centroid of the other points. This line is analyzed either by a simple bounded exponential search as suggested by Box or by a method involving successive quadratic approximations. If a point is found with a higher function value than the original defining point, it replaces the original point in the complex set. The first choice of defining point is the one with the lowest function value, but if it is not replaced by a point with higher function value than at least one point in the complex set, then all the other points are tried in order of increasing function value. If none of the points can produce an increase in function value, the sequence terminates, ideally with all of the points coinciding at the optimum.

The initial complex set is formed from any guesses or estimates of the optimum that may be available, filled in by randomly chosen points.

Constraints come in two forms: equality and inequality, and in a wide range of degrees of complexity that can be lumped into two levels: explicit and implicit, the distinction as far as the present case is concerned being that it is much easier to determine whether a given point satisfies an explicit constraint than it is to evaluate the function to be maximized, while the same is not true of an implicit constraint. The low-thrust trajectory optimization problem involves all four combinations of constraint types.

Explicit inequality constraints arise, for example, from the fact that a negative value for the length of any of the arcs into which the trajectory is divided would be physically meaningless. They are met by checking each point considered before evaluating the function, and rejecting the point unless all such constraints are met. These constraints turn out to provide upper and lower bounds for all of the variables that constitute the parameter space.

There is exactly one explicit equality constraint, expressing the fact that the lengths of the trajectory arcs must add up to the specified full length of the trajectory. It is eliminated by removing the length of the last trajectory arc from the parameter space and automatically giving it the value required to satisfy the equality constraint. As a result, the condition that the length of the last trajectory arc be non-negative becomes more complicated but remains an explicit inequality constraint.

Implicit inequality constraints arise because the path-generating process can fail in any of the arcs of the trajectory. For example, the trajectory can proceed along a hyperbolic asymptote and thus never reach the ecliptic longitude specified for the end of an arc. These constraints are satisfied by checking at each point considered during evaluation of the function, and rejecting the point (by assigning a very large negative value to the function) unless all such constraints are met.

The implicit equality constraints are the most troublesome. They are produced by the requirement that position and time at the end of the trajectory possess specified values. They are dealt with by modifying the function to be maximized, subtracting "penalty" functions of the errors in final position and time from the payload. By proper choice of parameters in the penalty functions, the optimizing process can be presented with a problem that amounts to first finding a solution to the constraint equations and then maximizing the payload subject to the constraints.

5. The Payload Formulas

The payload of the spacecraft is given by the following formulas:

$$M_{pl} = M_f \left[A_2 \exp(-dV_2/C_2) - B_2 \right], \qquad A_2 - B_2 = 1$$

$$M_f = M_0 - M_{pp} - M_p$$

$$M_p = M_0 \left[1 - \exp\left(\frac{-1}{I_{sp} g_s} \int_{\Phi_0}^{\Phi_f} \frac{\epsilon g_e a^2}{r^2} \frac{r \cos \Psi}{V_\Phi} \, d\Phi \right) \right]$$

$$M_{pp} = \frac{\alpha}{2\lambda} \epsilon_0 g_c I_{sp} g_s$$

$$M_0 = A_1 \exp(-dV_1/C_1) - B_1, \qquad A_1 - B_1 = M_i$$

Refer to Table 1 for definition of symbols.

6. Present Status and Future Plans

The complete ASTRAL program is presently in a checkout phase. As mentioned in Subsection 3, the PATH subroutine has already been checked out and its limitations identified. The next step is to check out the complete program with the exclusion of the optimizer. This is presently being done by simulating an ASTRAL trajectory on Carl Sauer's integrating low-thrust program[1] and making an initial check on the basic parameters. It will also determine the effect of assuming an inverse-square thrust acceleration and constant mass of the spacecraft.

[1]This program was used in recent Jupiter mission studies at JPL.

The next step in the checkout schedule will be to take a Sauer optimum trajectory and attempt to duplicate it. Once this is done, numerous ASTRAL runs will be generated in the vicinity to hand-pick an optimum; then a check will be made to see if ASTRAL will get the same optimum using the optimizer. This procedure will be followed to check out the optimizing scheme. Once past the checkout phase, ASTRAL will be ready to be used as a level-1 program.

A major extension to ASTRAL will be done later to implement it with William Stavro's solutions for arbitrary thrust-power laws. This is a study which investigates the general case where the thrust acceleration can vary as the inverse of the distance to the sun raised to some arbitrary power α. Thus, the value $\alpha = 0$ will signify constant-thrust acceleration (an approximation to the

Table 1. Nomenclature

A_1, B_1, C_1	constants describing initial high-thrust maneuvers
A_2, B_2, C_2	constants describing final high-thrust maneuvers
a	1 AU (149,597,892 km)
dV_1	velocity change in initial high-thrust maneuvers
dV_2	velocity change in final high-thrust maneuvers
g_c	acceleration of solar gravity at 1 AU (0.593 cm s^{-2})
g_s	standard acceleration of earth gravity (980.665 cm s^{-2})
I_{sp}	specific impulse of low-thrust propulsion system
$I_{sp}g_s$	effective exhaust velocity of low-thrust propulsion system
M_f	spacecraft mass just before final high-thrust maneuver (if any), e.g., insertion into orbit about target planet
M_i	spacecraft mass at parabolic orbital status relative to launch planet during initial high-thrust maneuver
M_p	propellant mass
M_{pl}	payload mass
M_{pp}	powerplant mass
M_0	spacecraft mass just after initial high-thrust maneuver, e.g., chemical boost from earth orbit
r	distance of spacecraft from sun
$r \cos \Psi / V_\Phi$	$(d\Phi/dt)^{-1}$, reciprocal of time derivative of Φ
V_Φ	ecliptic longitude component of spacecraft velocity
α	powerplant specific mass at 1 AU
ϵ	ratio of spacecraft thrust acceleration to acceleration of local solar gravity
$\epsilon g_c a^2/r^2$	thrust acceleration of spacecraft
ϵ_0	ratio of spacecraft thrust acceleration to acceleration of local solar gravity at 1 AU
λ	low-thrust propulsion system efficiency
Φ	ecliptic longitude of spacecraft
Φ_f	final value of Φ
Φ_0	initial value of Φ
Ψ	ecliptic latitude of spacecraft

nuclear–electric case), $\alpha = 2$ will parallel Wesseling's analysis, and $\alpha = 1.4$ will reflect recently proposed solar-electric propulsion systems to be used for missions to Jupiter.

References

1. Shi, Y., and Eckstein, M., "Ascent or Descent from Satellite Orbit by Low Thrust," *AIAA J.*, Vol. 4, pp. 2203–2209, 1966.
2. Wesseling, P., "A Two-Variable Asymptotic Solution for Three-Dimensional Solar Powered Low-Thrust Trajectories in the Vicinity of the Ecliptic Plane," *Astronaut. Acta*, Vol. 13, pp. 431–440, 1967.
3. Box, M. J., "A New Method of Constrained Optimization and a Comparison with Other Methods," *Comput. J.*, Vol. 8, pp. 42–52, 1965.

B. An Earth–Venus–Mercury Mission Opportunity in 1978, *F. M. Sturms, Jr.*

In a previous article (SPS 37-39, Vol. IV, pp. 1–5), it was reported that no favorable Earth–Venus–Mercury opportunity existed in 1978, and in particular that no energy match at Venus for the Earth–Venus and Venus–Mercury trajectory legs was possible for launch energies C_3 of less than 21 km²/s². At the time these results were reported, the *Atlas–Centaur* vehicle was unable to inject significant payloads (greater than 1000 lb) to energies higher than about 21 km²/s², and was the rationale for using this constraint. Larger boost vehicles then contemplated could easily deliver large payloads on direct Mercury missions, which require launch energies of about 50 km²/s² (Ref. 1).

More recently, uprating of the *Atlas–Centaur* vehicle, and the entry of a number of intermediate-size launch vehicles into the mission planning picture, require the consideration of higher launch energies. This fact has been reported by A. A. VanderVeen of Bellcomm, Inc., who has determined some preliminary trajectory characteristics.[2]

High-energy Earth–Venus–Mercury trajectories have been generated using JPL's multiple-planet conic program SPARC.[3,4] Figures 3–8 show some of the more important trajectory parameters. Figure 3 shows the region of possible trajectories on a Venus arrival date versus Earth launch date grid. Figures 4–8 show the

[2] *Preliminary Results of an Attractive Earth–Venus–Mercury Mission in 1978*, Bellcomm, Inc., Washington, D.C., Oct. 9, 1968 (internal memorandum).

[3] Joseph, A. E., and Richard, R. J., *Space Research Conic Program*, July 1966 (JPL internal document).

[4] Derderian, M., *Space Research Conic Program, Phase III*, Apr. 1968 (JPL internal document).

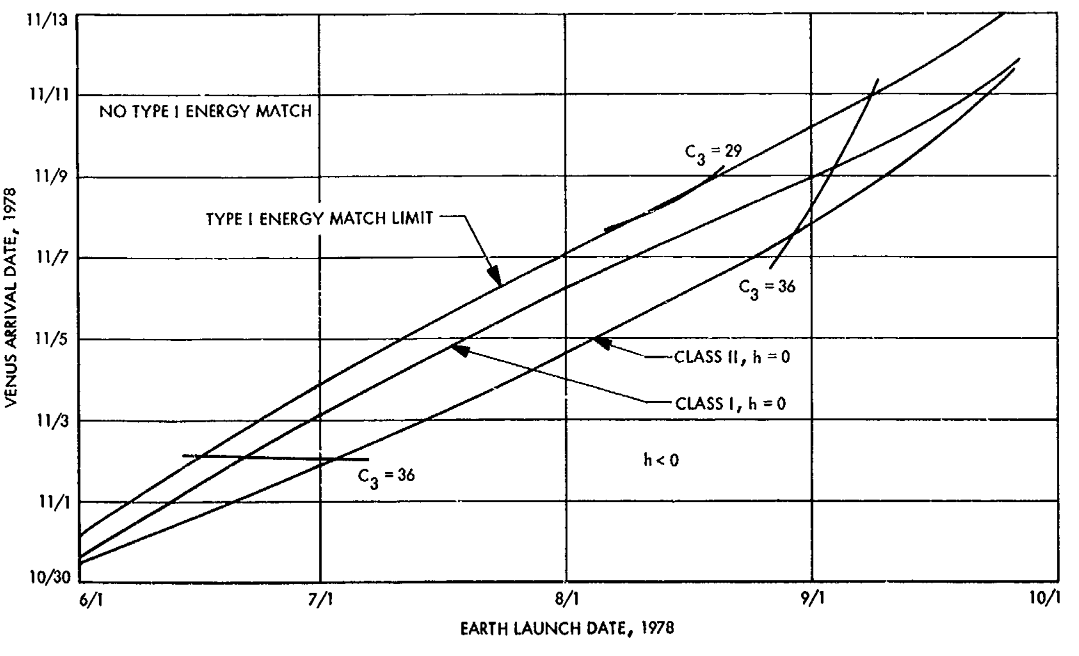

Fig. 3. Region of possible trajectories on a Venus arrival date vs Earth launch date grid

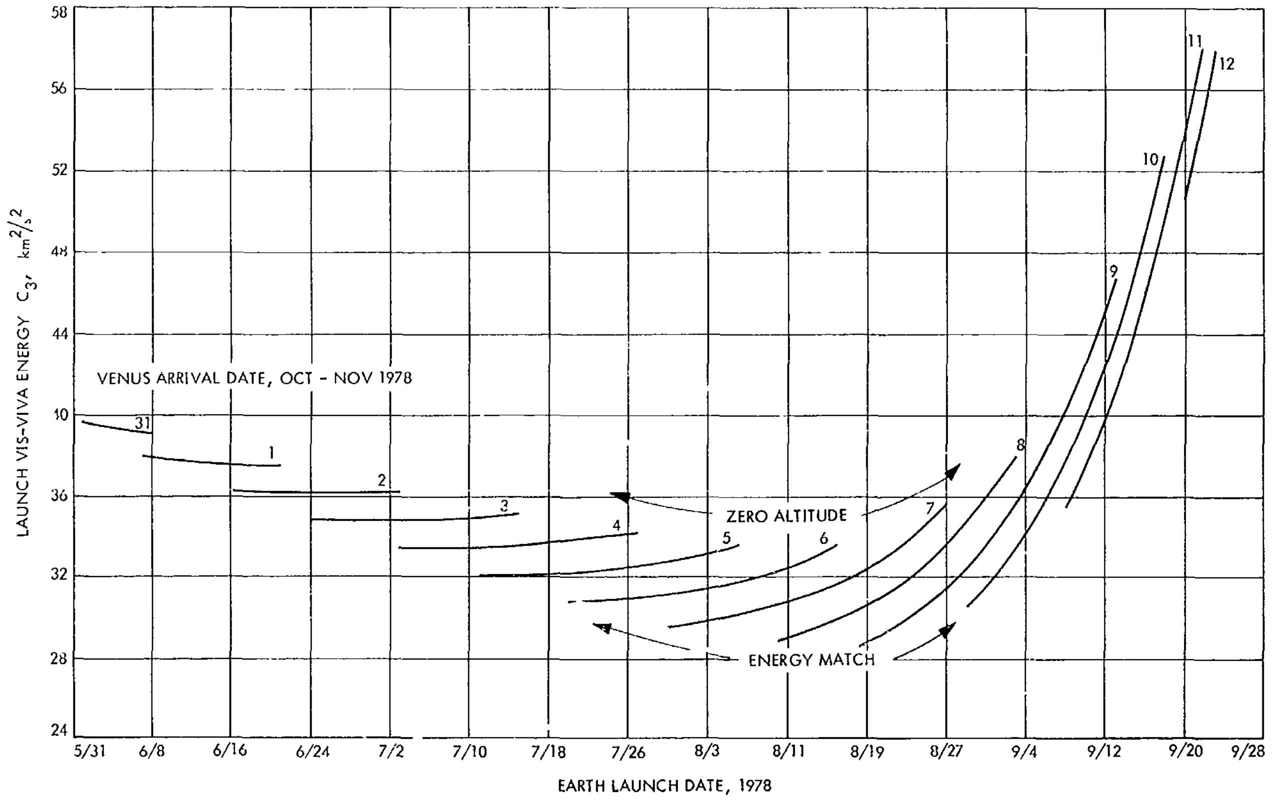

Fig. 4. Launch energy vs Earth launch date

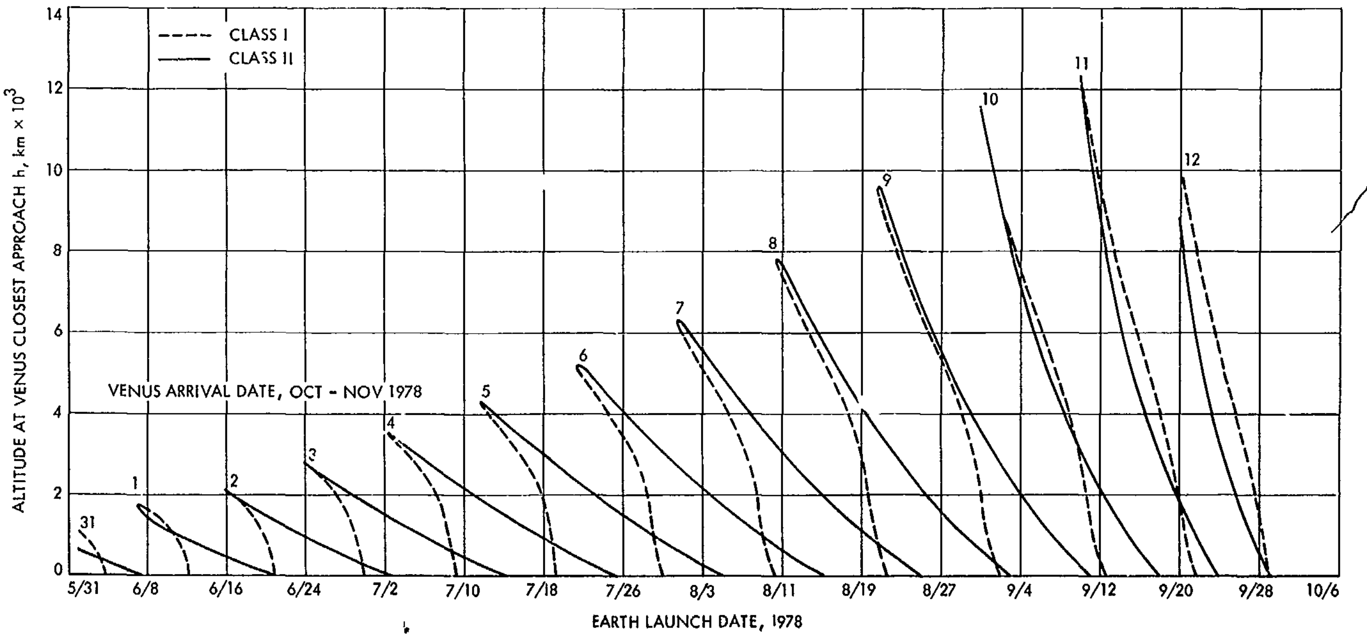

Fig. 5. Altitude of Venus closest approach vs Earth launch date

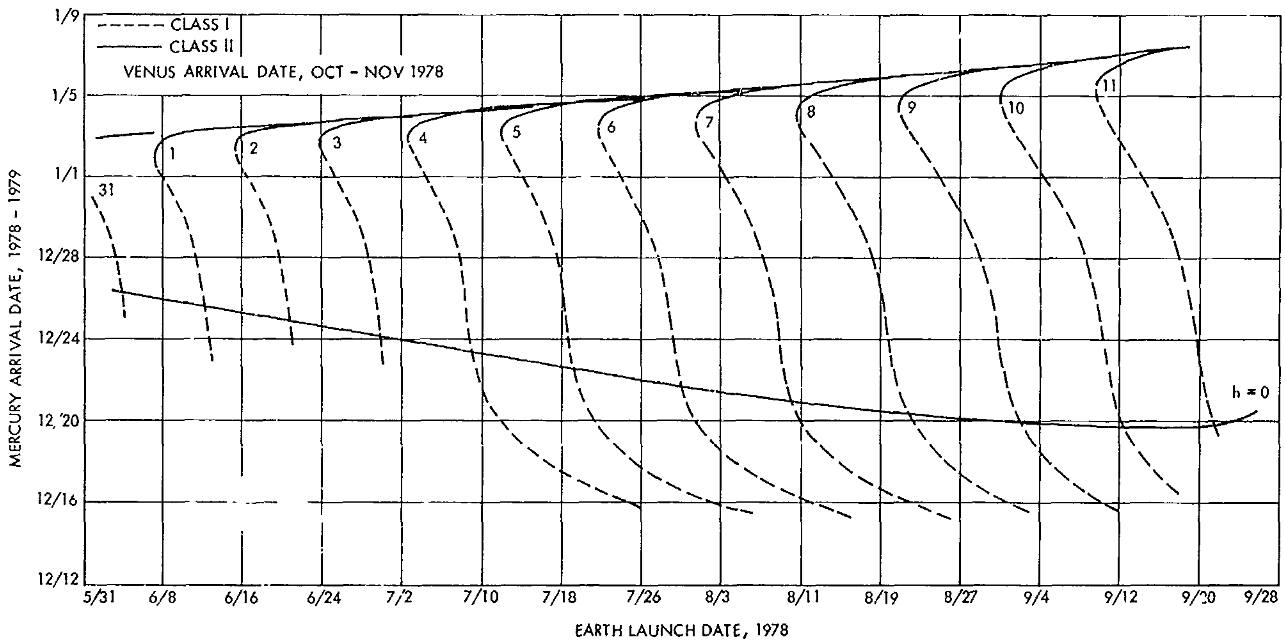

Fig. 6. Mercury arrival date vs Earth launch date

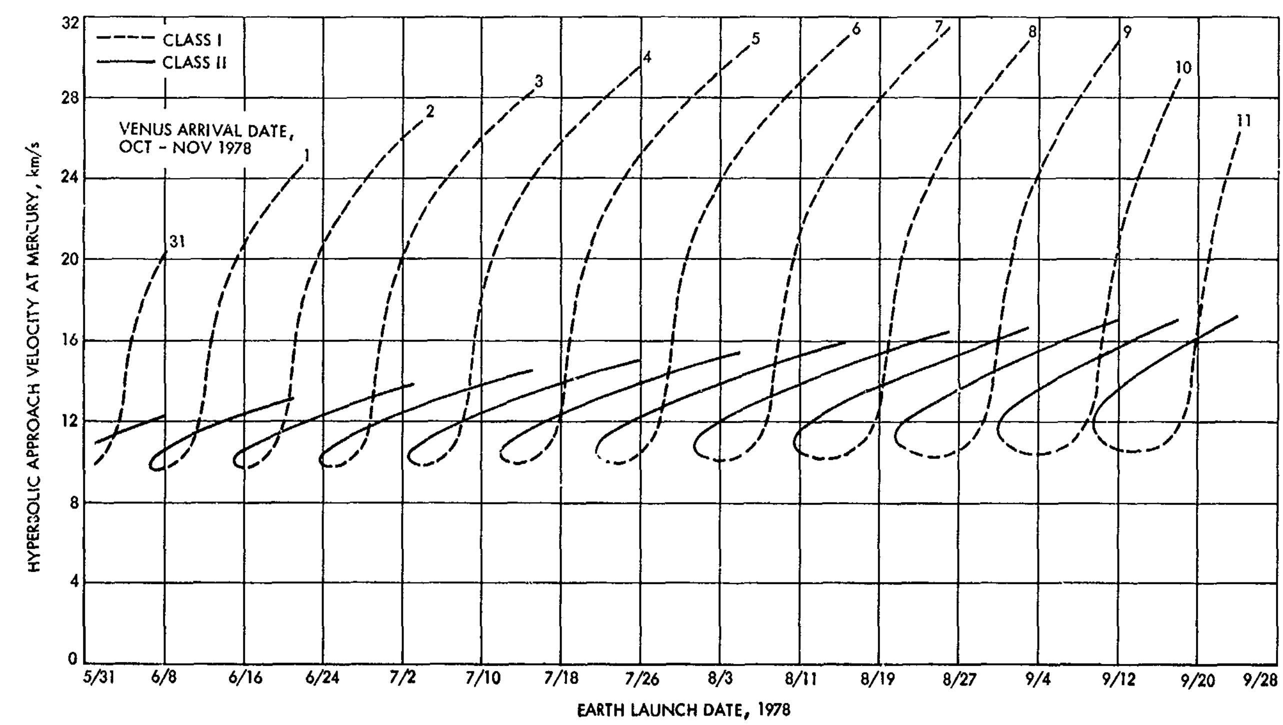

Fig. 7. Hyperbolic approach velocity at Mercury vs Earth launch date

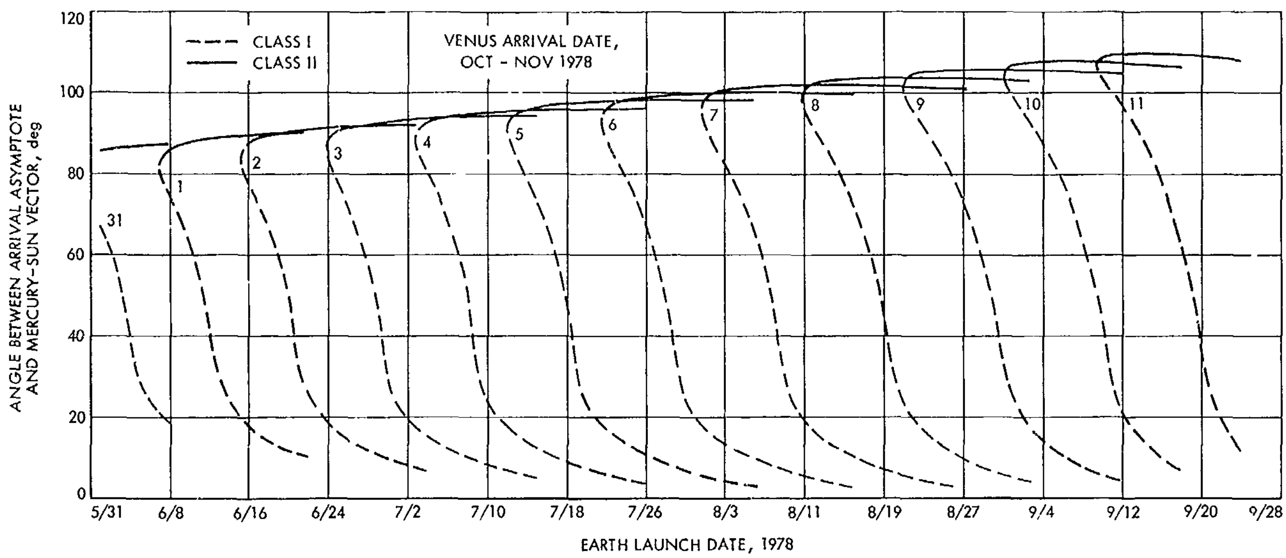

Fig. 8. Angle between arrival asymptote and Mercury–Sun vector vs Earth launch date

following quantities plotted versus Earth launch date, using a constant Venus arrival date as a parameter:

(1) Launch energy C_3.

(2) Altitude of closest approach h at Venus (Venus radius taken as 6080 km).

(3) Mercury arrival date.

(4) Hyperbolic approach velocity at Mercury.

(5) Angle between arrival asymptote and Mercury–Sun vector (determines lighting for Mercury photography).

A launch energy of 35 km²/s² will produce an adequate launch period. Table 2 shows current payload estimates for several launch vehicles for energies of 35 and 50 km²/s². These performance values were obtained from Ref. 2, except for the SLV-3X/*Centaur* value.

Using the values in Table 2, the SLV-3C/*Centaur* and *Titan* 3C vehicles appear marginal for the 1978 Venus–Mercury mission. The addition of a *Burner II* stage to these vehicles increases the payload to where both the indirect 1978 Venus–Mercury and direct Mercury missions are attractive. The SLV-3X/*Centaur* vehicle is a possible choice for the Venus–Mercury mission in 1978.

Predicted launch-vehicle performance values change frequently, thus affecting the attractiveness of given missions. The values given above indicate that serious consideration should now be given to the 1978 Earth–Venus–Mercury mission opportunity in comparison to more favorable but earlier Venus–Mercury opportunities, and in comparison to direct Mercury missions.

References

1. Clarke, V. C. Jr., et al., *Design Parameters for Ballistic Interplanetary Trajectories, Part II. One-Way Transfers to Mercury and Jupiter*, Technical Report 32-77. Jet Propulsion Laboratory, Pasadena, Calif., Jan. 15, 1966.
2. *Mission Planners Guide to the Burner II*, Report D2 82601-5, The Boeing Co., Seattle, Wash., Apr. 1968.

Table 2. Launch vehicle payloads for two launch energies

Launch vehicle	Payload for $C_3 = 35$ km²/s² (1978 Venus–Mercury), lb	Payload for $C_3 = 50$ km²/s² (direct Mercury), lb
SLV-3C/*Centaur*	750	50
SLV-3C/*Centaur*/*Burner II*	1400	1000
Titan 3C	800	0
Titan 3C/*Burner II*	2250	1500
SLV-3X/*Centaur*[a]	1100	200

[a]Williams, A. N., *Launch Vehicle Data Book*, Aug. 30, 1968 (JPL internal memorandum).

C. Trajectory Analysis of a 1975 Mission to Mercury via an Impulsive Flyby of Venus,[5]

R. A. Wallace

1. Introduction

The concept of using gravitational fields to significantly alter the energy and direction of interplanetary trajectories is not a new one. In 1963, M. A. Minovitch proposed several interesting interplanetary missions using this multiple-planet flyby concept (Ref. 1). The advantages of this form of mission are the savings in launch energy and the increase of data return associated with the "two planets for the price of one" idea. It is not surprising, therefore, that a great deal of interest has been generated in multiple-planet flyby missions and, in particular, missions to Mercury via Venus in the 1970's. Direct ballistic trajectories to Mercury generally require launch energies of 45 km^2/s^2 or more, while multiple-planet trajectories to Mercury are available which require less than 30 km^2/s^2.

There are six attractive opportunities for Earth–Venus–Mercury missions during the remainder of the century; these are listed in Table 3. An attractive opportunity is one for which either an *Atlas/Centaur* or *Titan III* launch vehicle can be used to launch a payload of more than 800 lb (i.e., corresponding to an upper limit of launch energy of 33 km^2/s^2). Although the 1970 and 1973 opportunities are excellent, they may not be available because of program considerations. The next opportunity is in 1975, but is plagued with very low Venus closest-approach altitudes. The study summarized here investigates the feasibility of using a small propulsive assist at Venus to allow reasonable Venus flyby altitudes and thereby increase the attractiveness of the 1975 opportunity.

Results of the study are presented in three parts. First, a very brief discussion is given on the general single-impulse flyby analysis which permits the analyst to investigate in detail the impulse requirements of multiple-planet trajectories utilizing propulsive assist. Secondly, an efficient procedure is outlined for the application of the above analysis to the 1975 Earth–Venus–Mercury mission. The final subsection is devoted to the mission design and analysis for the 1975 Earth–Venus–Mercury opportunity.

2. Single-Impulse Flyby Analysis

The analysis used is simple and can be applied to any multiple-planet trajectories where propulsive assist may

[5]This article is a summary of Ref. 2.

Table 3. Earth–Venus–Mercury mission opportunities (ballistic flyby)

Launch year	Launch energy, km^2/s^2	Venus closest-approach altitudes, km
1970	14	3000
1973	19	5000
1975	21	Less than 700
1982	24	2000
1994	24	1400
1998	16	3600

help in raising closest approach altitudes or taking advantage of particular interplanetary trajectory characteristics, such as reduced flight time. The analysis uses three input control parameters:

(1) Launch and arrival dates (fixes the approach and departure asymptotic velocity vectors).

(2) Closest approach altitude.

(3) Maneuver radius.

These parameters are thought to be the most practical choice of control variables for operating a multiple-planet mission requiring propulsive assist. They also make up a minimum set required to uniquely determine the trajectories at encounter (Fig. 9). The analysis could be carried out two-dimensionally because of the principal constraint of requiring the trajectories to contain the two determining asymptotic velocities. Details of the solution are given in Ref. 2.

3. Application of Single-Impulse Flyby Analysis

The single-impulse flyby analysis was applied to the region of the 1975 Earth–Venus–Mercury opportunity which exhibited relatively low launch energies and maximum Venus closest-approach altitudes. In a perliminary study, certain factors became evident:

(1) The Venus arrival time is very important in obtaining low impulse maneuvers (sensitivity: 20 m/s/h).

(2) The ΔV is relatively invariant with maneuver radius *for* optimum choice of Venus arrival time. (For non-optimal times, ΔV could vary as much as ⅓ of its minimum value.)

The ΔV sensitivity with Venus arrival time is explained by the fact that the Venus closest-approach altitude was kept constant. It was found, however, that the ΔV sensitivity to closest-approach altitude is also quite high,

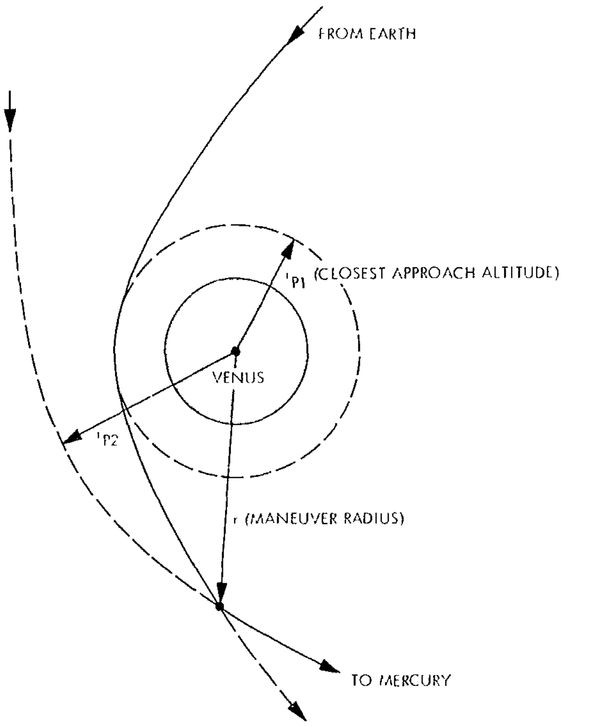

Fig. 9. Encounter trajectories in orbit planet

about 60 m/s for every 100-km change in altitude. Thus, the ΔV sensitivity to Venus arrival time could be softened by changing the Venus flyby altitude with Venus arrival time. It was decided, however, that a minimum acceptable altitude of 1000 km should be used throughout the study. If further decreases were allowable, the savings of 60 m/s for every 100-km decrease could be realized up to a point where too much trajectory bending results and ΔV increases.

In the preliminary study, ΔV was found to be very insensitive to maneuver radius for the optimum choice of Venus arrival times. This is because the two encounter orbits, approach and departure, are almost identical and the velocity differences are almost constant with maneuver radius. One orbit can be thought of as a perturbation of the other because the impulse required is small compared to the orbital velocities (9 to 13 km/s). For non-optimum choice of Venus arrival time, the angle between the two orbits is larger than for the optimum arrival time, although the orbits are almost identical in other respects. The above observations are not applicable at periapsis where the velocity differences are most pronounced.

Since ΔV is almost constant with change in maneuver radius for optimum Venus arrival times, attention during the rest of this study will be restricted to maneuvers performed on the asymptotes (i.e., at about encounter plus or minus several days). There are four major advantages that result from such a policy:

(1) The required impulse can be combined with one of the error-correction maneuvers, resulting in smaller execution errors and greater reliability for fewer maneuvers.

(2) The Venus encounter experiments could be given full operational consideration and not complicated by a maneuver.

(3) A continuous tracking data fit could be acquired throughout encounter, reducing orbit determination errors for the post-encounter error-correction maneuver.

(4) The impulse was found to be smallest at large distances from Venus for the final design trajectories.

Considering these points, the remainder of the discussion is confined to results concerning asymptotic maneuvers.

To define a mission, design charts are required which will clearly show the tradeoffs in the important parameters involved. In the construction of design charts, the first step is to optimize Venus arrival time. Figure 10 is an example of the many plots required in the optimization procedure.

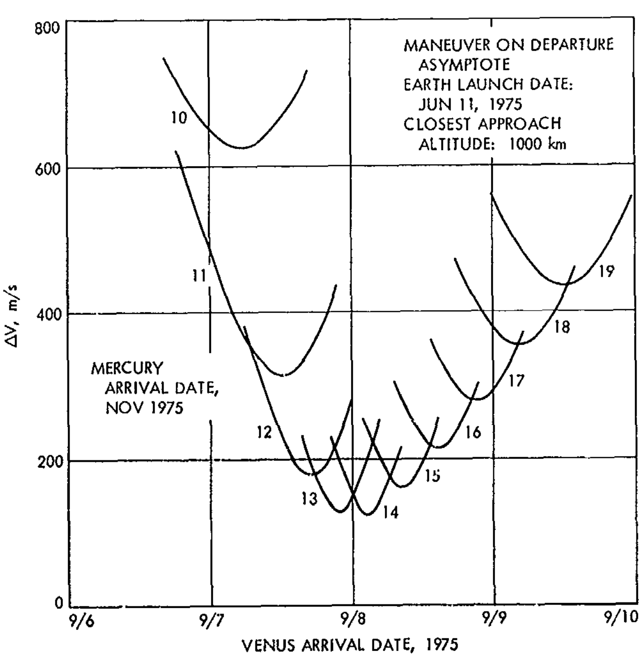

Fig. 10. Maneuver impulse ΔV vs Venus arrival date (Mercury arrival date varied)

Design charts were constructed for maneuvers performed on both the approach and departure asymptotes with Venus arrival time and launch energy as parameters overlayed on the basic ΔV contour chart. Note that all points used in the design charts are for the optimum Venus arrival time. Figure 11 is the design chart for maneuvers performed on the departure asymptote with launch energy as an overlay. It was found that maneuvers performed on the departure asymptote resulted in generally lower ΔV's than those on the approach asymptotes.

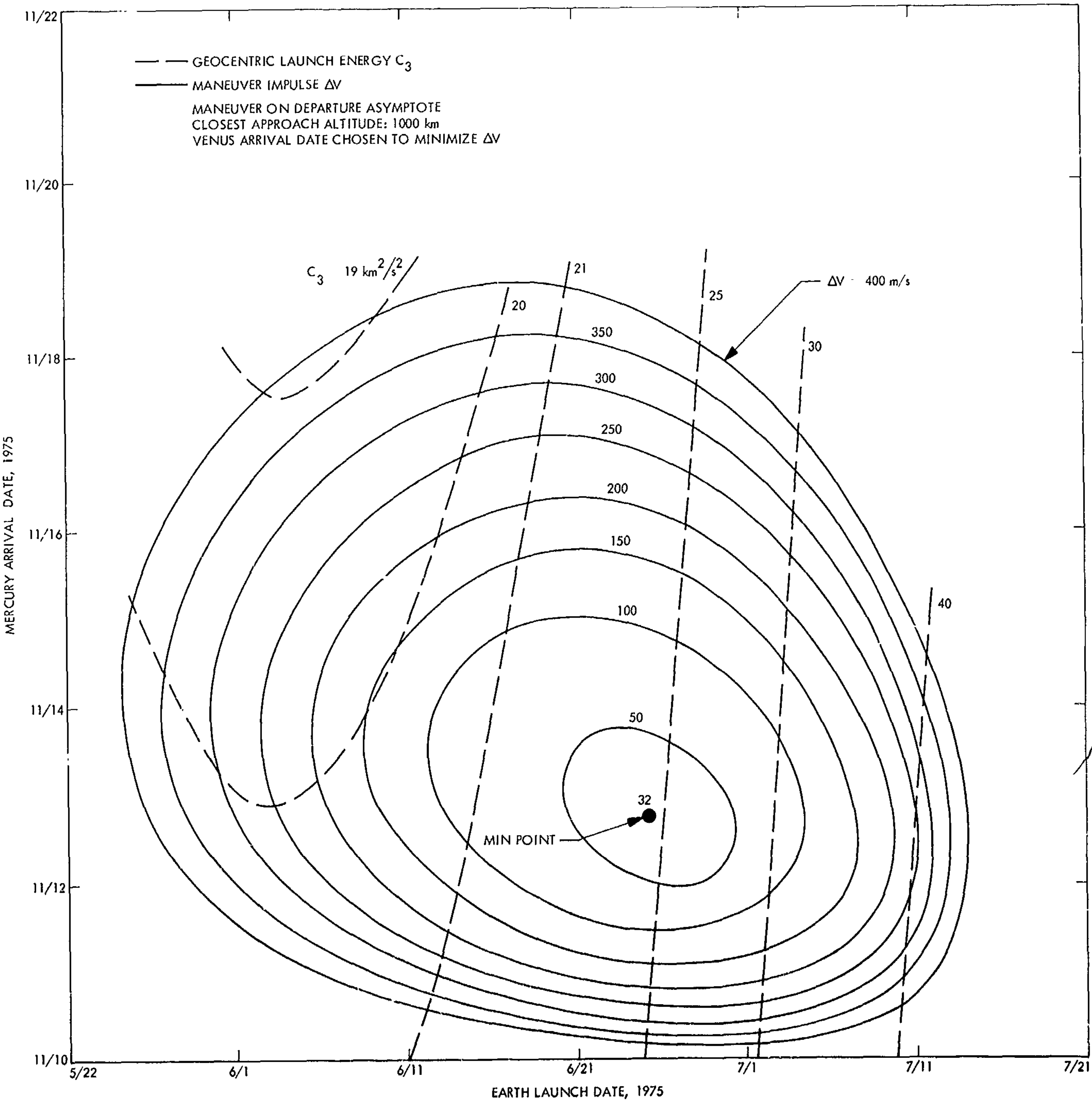

Fig. 11. Earth–Venus–Mercury mission design chart: launch energy C_3 and maneuver impulse ΔV

This is due to the departure speeds being generally higher than the approach speeds (a slower speed at encounter results in greater bending of the trajectory).

4. 1975 Earth–Venus–Mercury Mission Design

Using Fig. 11, the basic design chart, two missions were designed: one requiring low launch energies, the other, low propulsive assist at Venus. There is a definite launch vehicle and ΔV tradeoff available. The low launch-energy mission design is characterized by:

(1) Launch energy ≤ 21 km^2/s^2 (*Atlas/Centaur*).

(2) $\Delta V \leq 350$ m/s.

(3) 20-day launch period (May 27 to June 16, 1975).

(4) Mercury arrival time: Nov. 14, 1975.

The low propulsive-assist mission is characterized by:

(1) Launch energy ≤ 30 km^2/s (*Titan III*).

(2) $\Delta V \leq 100$ m/s.

(3) 20-day launch period (June 12 to July 2, 1975).

(4) Mercury arrival time: Nov. 13, 1975: 12 h.

Note the existence of two attractive mission designs, one requiring more onboard propulsion, but a smaller launch vehicle. Both missions require relatively small impulses when measured against the total ΔV usually required on ballistic multiple-planet missions.

As observed in the preliminary study, ΔV, as shown in Fig. 12 for the low propulsive-assist mission design, is almost constant with maneuver radius, being slightly higher near encounter. The characteristic of ΔV being higher at encounter is due to the dominating angular momentum or orientation requirements.

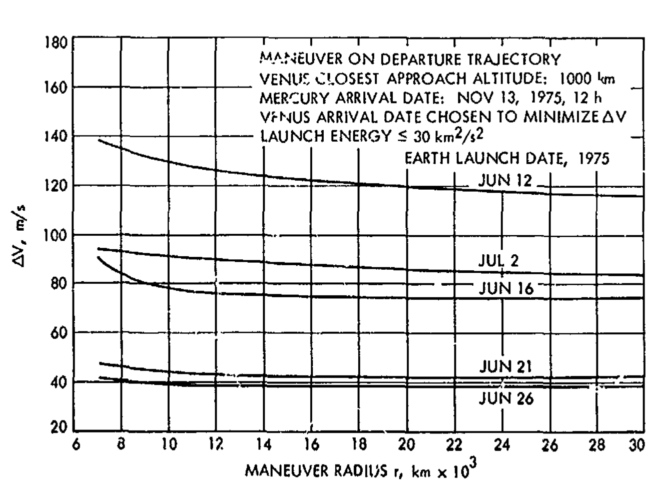

Fig. 12. Low propulsive-assist mission design: maneuver impulse ΔV vs maneuver radius r

Encounter conditions at Venus result in Earth occultation for all launch days in both mission designs. Figure 13 is a plot of the Venus occultation regions for a representative launch day. Note the 3σ error ellipse resulting from a 0.1-m/s spherically distributed midcourse execution error at launch + 5 days. The crossing of this ellipse into the impact zone indicates that a pre-encounter error-correction maneuver is required (a common requirement for multiple-planet missions), and that reducing the Venus closest-approach altitude much below 1000 km may be impractical.

Launch conditions for both mission designs are very good. The characteristics are:

(1) Launch azimuth corridors of 90 to 114 deg.

(2) Launch windows $\geq 2\frac{1}{4}$ h.

(3) Parking orbit coast times: 12 to 16 min (compatible with both the *Atlas/Centaur* and *Titan III* launch vehicles).

(4) Injection over mid-Atlantic to South Africa (reasonable near-earth tracking requirements for the Air Force Eastern Test Range).

For any study which is dependent on conic analysis, it is important that an accurate check be made on the final results. A comparison of the conic results with the precision integrated data is given in Table 4. The integrated data was supplied by the SPACE trajectory program (Ref. 3), a program used with a high degree of accuracy on actual missions to Mars, the moon, and Venus. Errors of between 8 and 13 m/s in ΔV are shown and point to the accuracy which may be realized with conic analyses if relative values (e.g., velocity differences) are required rather than absolute values.

References

1. Minovitch, M. A., *The Determination and Characteristics of Ballistic Interplanetary Trajectories Under the Influence of Multiple Planetary Attractions*, Technical Report 32-464. Jet Propulsion Laboratory, Pasadena, Calif., Oct. 31, 1963.

2. Wallace, R. A., "Trajectory Analysis of a 1975 Mission to Mercury via an Impulsive Flyby of Venus," Paper 68-113, presented at the AAS/AIAA Astrodynamics Specialists Conference, Jackson, Wyoming, Sept. 3–5, 1968.

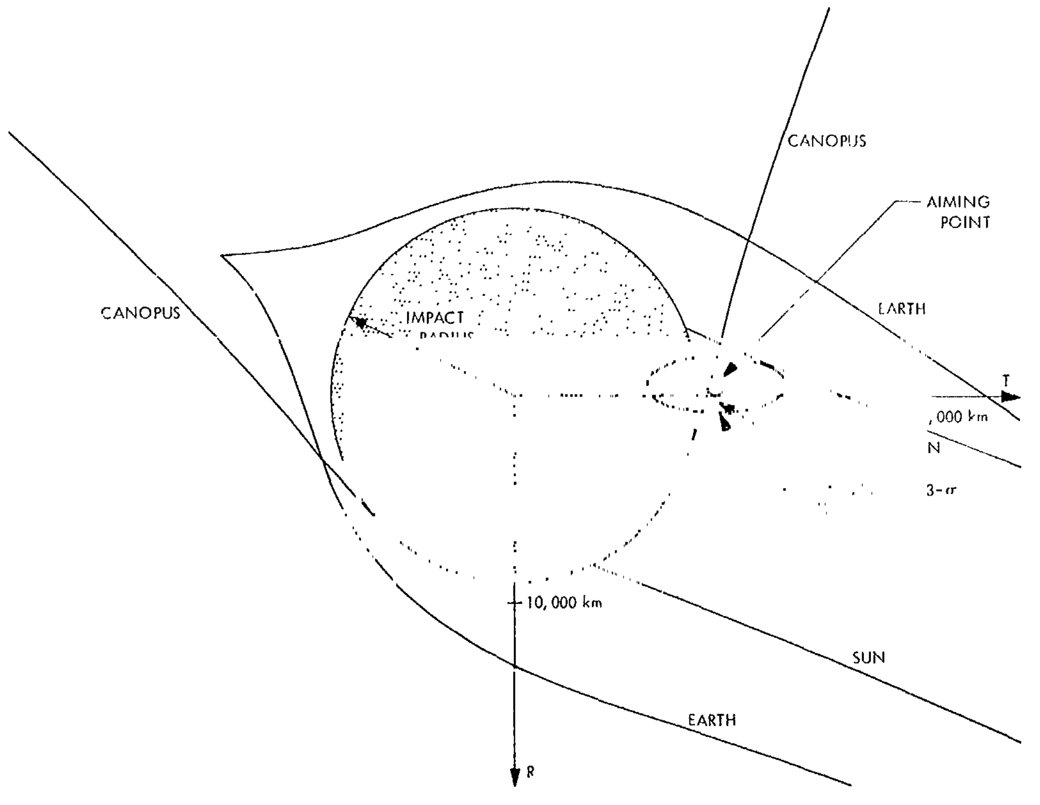

Fig. 13. Venus occultation zones (earth launch: Jun. 11, 1975; Venus arrival: Sept. 8, 1975, 3 h)

Table 4. Conic results vs integrated trajectory program data for various launch dates

Parameter	May 27, 1975		June 11, 1975		July 2, 1975	
	Conic	Integrated	Conic	Integrated	Conic	Integrated
b, km	10,333.96	10,333.14	10,079.9	10,081.89	9766.6	9767.3
θ, deg	353.91	353.91	357.00	357.01	0.42	0.43
VHP, km/s	9.0100	9.1102	9.4529	9.5586	10.0815	10.2069
VHL, km/s	9.2155	9.3370	9.5282	9.6373	10.1075	10.2289
r_p, km	7080.0	7079.7	7080.0	7081.4	7080.0	7080.4
i, deg[a]	8.62	13.10	4.05	1.43	1.48	94.44
I, deg[a]	3.420	3.410	3.406	3.403	3.436	3.436
Ω, deg[a]	31.92	30.72	35.60	36.21	246.83	209.15
ΔV, m/s	368.8	360.5	131.0	122.9	79.8	66.9

[a]Post-maneuver.

[b]b = impact parameter, hyperbolic semiminor axis; θ = targeting angle in B-plane; VHP = approach asymptotic speed on uncorrected trajectory; VHL = departure asymptotic speed required on departure trajectory; r_p = closest approach distance; i = orbital inclination to the ecliptic, Venus-centered; I = heliocentric inclination to the ecliptic of Venus–Mercury trajectory; Ω = longitude of the ascending node; ΔV = required impulse.

3. White, R. J., et al., *Space Single Precision Cowell Trajectory Program*, Technical Memorandum 33-198. Jet Propulsion Laboratory, Pasadena, Calif., Apr. 15, 1965.

D. Missions to the Outer Planets, *R. A. Wallace*

The 1975 to 1980 time period will afford an unusually favorable opportunity to launch missions to explore all of the outer planets. During this time period, the planetary geometries are such that rare multiple-planet missions involving all the major planets are possible. Such opportunities will not occur again for almost two centuries. This article expands on opportunities previously identified (SPS 37-35, Vol. IV, pp. 12–23) to show energy requirements and other characteristics for realistic launch periods.

Table 5 is a summary chart of eleven missions to the outer planets with launch opportunities from 1976 through 1979.[6] A comprehensive plan to explore all of the outer planets of the solar system could be constructed from this chart. There are four types of missions included:

(1) Single-planet missions: direct missions to Saturn, Uranus, Neptune, and Pluto (four missions).

(2) Two-planet mission: Earth–Jupiter–Pluto (one mission).

(3) Three-planet missions (grand tour minus Saturn): Earth–Jupiter–Uranus–Neptune (two missions).

(4) Four-planet missions (grand tour): Earth–Jupiter–Saturn–Uranus–Neptune (four missions).

Each of the eleven missions shown in Table 5 have been designed with consideration given to launch energy, time of flight, launch period, planetary flyby altitudes, and launch conditions.

The Rings of Saturn may present a formidable obstacle to spacecraft flying by that planet at altitudes less than 150,000 km. The present physical model of the Rings is much in doubt, however, and trajectories passing between the top of the atmosphere and the interior Ring or passing at altitudes greater than 70,000 km may be possible. The 1977 interior Ring passage grand tour mission (1977 Jupiter–Saturn interior Ring–Uranus–Neptune) would be most desirable. If a Saturn flyby altitude of 150,000 km were required, then a flight duration of 13 yr would result. If two spacecraft were available and the risks of catastrophic impact with the Rings of Saturn were found to be high for desirable grand tour missions, then one of the three-planet missions might be used in addition to a grand tour.

There is no question that a mission to Saturn, Uranus, Neptune, or Pluto should be flown with the aid of the gravitational field of Jupiter and/or Saturn. The 1977 Earth–Jupiter–Pluto opportunity is the best of five possible beginning in 1975 and ending in 1979 (Ref. 5). There are Earth–Saturn–Pluto missions available, but the launch energy is 140 km^2/s^2 or more. Launch energies for direct missions to Saturn begin to decrease in 1980 until in 198[illegible] [illegible] launch energy of 130 km^2/s^2 is sufficient for a 15-day launch period.

A sample plan to explore the outer planets by launching missions before 1980 might be the following:

(1) 1977 grand tour (interior Saturn Ring passage).

(2) 1978 grand tour minus Saturn.

Alternate missions in case of launch failure might be:

(1) 1978 grand tour (exterior Saturn Ring passage).

(2) 1979 grand tour minus Saturn.

---

[6]Earth–Jupiter missions are discussed in Refs. 1 and 2 and in JPL Engineering Planning Document 358, which provides data on launch opportunities from 1974 to 1981. The grand tour (four-planet) missions were designed by L. Kingsland (Ref. 3). The other missions in Table 5 are from unpublished material by the author. All missions but two were designed with the aid of a patched conic computer program SPARC [Derderian, M., *Space Research Conic Program, Phase III*, April 1968 (JPL Internal Document)]. The data for the two 1977 grand tour (four-planet) missions were computed with the aid of a precision integrating program SPACE (Ref. 4).

References

1. Wallace, R. A., *Trajectory Considerations for a Mission to Jupiter in 1972*, Technical Memorandum 33-375. Jet Propulsion Laboratory, Pasadena, Calif., Mar. 15, 1968.

2. Clarke, V. C., et al., *Design Parameters for Ballistic Interplanetary Trajectories, Part II. One-Way Transfers to Mercury and Jupiter*, Technical Report 32-77. Jet Propulsion Laboratory, Pasadena, Calif., Jan. 15, 1966.

3. Kingsland, L., "Trajectory Analysis of a Grand Tour Mission to the Outer Planets," AIAA 5th Annual Meeting and Technical Display, pp. 68–1055, Philadelphia, Pa., Oct. 21–24, 1968.

4. White, R. J., et al., *SPACE Single Precision Cowell Trajectory Program*, Technical Memorandum 33-198. Jet Propulsion Laboratory, Pasadena, Calif., Apr. 15, 1965.

5. Flandro, G. A., "Fast Reconnaissance Missions to the Outer Solar System Utilizing Energy Derived from the Gravitational Field of Jupiter," *Astronaut. Acta*, Vol. 12, No. 4, Princeton, N.J., 1966.

Table 5. Missions to the outer planets

Characteristics	1976 Jupiter–Saturn interior Ring–Uranus–Neptune	1977 Jupiter–Saturn interior Ring–Uranus–Neptune	1977 Jupiter–Saturn exterior Ring–Uranus–Neptune	1978 Jupiter–Saturn exterior Ring–Uranus–Neptune	1978 Jupiter–Uranus–Neptune	1979 Jupiter–Uranus–Neptune	1977 Jupiter–Pluto	1979 Saturn (direct)	1977–1978 Uranus (direct)	1977 Neptune (direct)	1976 Pluto (direct)
Launch period, days	15	15	15	15	15	15	15	15	15	15	15
Maximum launch energy required, km^2/s^2	104	120	100	108	110	110	110	140	139	150	180
Capability for *Titan III/Centaur* (spacecraft weight; 114-deg azimuth), lb[a]	1400	780	1530	1250	1190	1190	1190	140	150	0	–
Capability for *Titan III/Centaur Burner II* 1440 (spacecraft weight; 114-deg azimuth, lb[a]		1380	1800	1620	1580	1580	1580	900	930	700	–
Maximum declination at launch (absolute value), deg	14	27	33	33	32	27	28	37	7	4	26
Jupiter encounter Flight time from launch, days Flyby altitude, km (Jupiter surface radius) Communication distance, km $\times 10^6$	 561 16,000 (0.2) 675	 511 212,000 (3.0) 638	 652 622,000 (8.8) 900	 593 1,600,000 (22.5) 767	 564 62,000 (0.9) 719	 579 560,000 (7.8) 749	 551 236,000 (3.3) 673	–	–	–	–
Saturn encounter Flight time from launch, days (yr) Flyby altitude, km (Saturn surface radius) Communication distance, km $\times 10^6$	 1363 (3.7) 8,000 (0.1) 1277	 1095 (3.0) 6,000 (0.1) 1562	 1394 (3.8) 75,000 (1.2) 1453	 1240 (3.4) 80,000 (1.3) 1321	–	–	–	 1255 (3.4) Open 1310	–	–	–
Uranus encounter Flight time from launch, days (yr) Flyby altitude, km (Uranus surface radius) Communication distance, km $\times 10^6$	 2798 (7.7) 32,000 (1.3) 2781	 2342 (6.4) 16,000 (0.7) 2910	 2945 (8.1) 86,000 (3.8) 2900	 2764 (7.6) 121,000 (5.1) 2717	 2293 (6.6) 22,000 (0.9) 2972	 2286 (6.3) 41,000 (1.7) 2833	–	–	 3092 (8.5) Open 2709	–	–
Neptune encounter Flight time from launch, days (yr) Flyby altitude, km Communication distance, km $\times 10^6$	 3894 (10.7) Open 4519	 3372 (9.2) Open 4613	 4100 (11.2) Open 4587	 4030 (11.0) Open 4642	 3503 (9.6) Open 4440	 3599 (9.9) Open 4457	–	–	–	 6209 (17.0) Open 4659	–
Pluto encounter Flight time from launch, days (yr) Flyby altitude, km Communication distance, km $\times 10^6$	–	–	–	–	–	–	 3500 (9.6) Open 3919	–	–	–	 15,231 (41.7) Open 4934

[a]J. Long, private communication.